Korean Journal of Chemical Engineering
https://doi.org/10.1007/s11814-024-00249-4

REVIEW ARTICLE (INVITED ONLY)

Wet Chemistry Methods for Synthesizing High-Entropy Nanoparticles: A Review of the Synthesis Strategies and Various Applications

Hyeonseok Lee[1] · Heesoo Jeong[1] · Wooseok Jeong[1] · Yun Jae Hwang[1] · Boeun An[1] · Yeongbin Lee[1] · Gyuhyeon Kim[1] · Don-Hyung Ha[1]

Received: 10 May 2024 / Revised: 24 July 2024 / Accepted: 29 July 2024

Abstract
High-entropy nanoparticles (HE-NPs) have recently gained considerable attention owing to their potential to yield several materials with unique characteristics due to the homogeneous mixing of five or more elements. The complexity of HE-NPs leads to electronic hybridization, lattice distortion, and sluggish diffusion effects, all of which contribute to their performance and stability. The formation of HE-NPs is thermodynamically limited, particularly by enthalpic factors. To overcome these limitations and design intricate nanostructures, wet chemistry can be employed as a relatively straightforward synthesis method. This review provides an overview of HE-NPs, including their definition, thermodynamic principles, and wet-chemical synthesis methods. It further explores the diverse range of applications of HE-NPs and examines how specific nanoparticle morphologies and compositions can be tailored efficiently using various synthesis strategies. Additionally, this review discusses case studies presenting optimized HE-NPs for individual applications, demonstrating their high performance. By identifying the key factors that contribute to their superior performance, this review offers valuable insights into future research directions for HE-NPs.

Hyeonseok Lee and Heesoo Jeong have equally contributed to this work.

✉ Don-Hyung Ha
dhha@cau.ac.kr

[1] School of Integrative Engineering, Chung-Ang University, 84 Heukseok-ro, Dongjak-gu, Seoul 06974, Republic of Korea

Published online: 18 August 2024

Graphical abstract

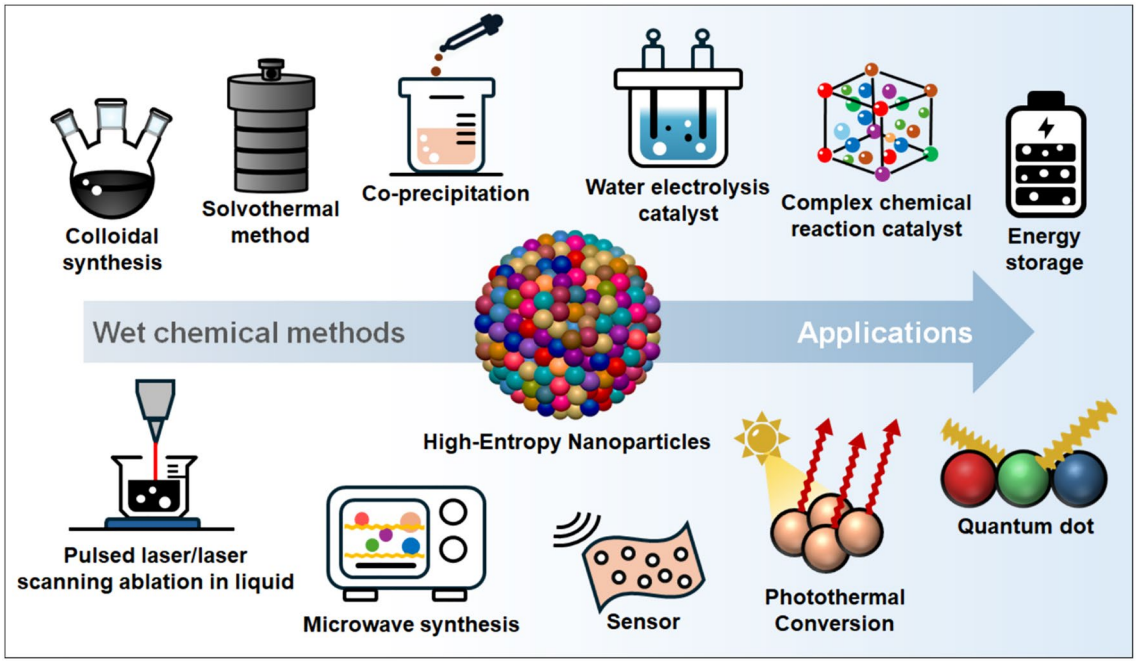

Keywords High entropy · Nanoparticles · Wet chemical · Colloidal synthesis · Water electrolysis catalyst · Co-precipitation

Introduction

The development of advanced materials with high complexity is a crucial research topic in modern material engineering to satisfy its functional demands. The unique characteristics of HE-NPs enable discovering materials with numerous combinations, offering the ability to design efficient nanostructures by controlling factors, such as constituent elements, synthesis methods, and compositions [1]. The first high-entropy alloy (HEA) was reported in 2004, and HE-NPs have since evolved primarily in the field of catalysis, demonstrating a high performance owing to the broadening of the d-band center characteristics of multi-element alloys and various reaction pathways [1–4]. Subsequently, the synthesis of various HE-NPs, including high-entropy oxides (HEO) [5–8], sulfides [9–11], carbides [12, 13], and borides [14, 15] has been reported, and their application fields are gradually expanding.

In this regard, the synthesis methods of HE-NPs are evolving to create NPs with more than five uniformly mixed elements, possessing properties suitable for various industrial applications [16–18]. Despite the recent advancements, the manufacturing of HE-NPs remains challenging, because each element exhibits different reduction rates and enthalpies, hindering a uniform element distribution and causing phase-separation or ordering during nanoparticle synthesis [19, 20]. Non-equilibrium synthesis using wet chemistry may solve these problems. Wet chemical methods, such as colloidal synthesis, co-precipitation, and solvothermal methods, have the advantage of being able to synthesize nanoparticles via a relatively low-temperature and simple process, and can be applied to the existing nanoparticle synthesis methods [21, 22]. Strategies for the synthesis of HE-NPs at low temperatures are primarily based on rapid chemical reaction rates. Metal precursors have different precipitation rates, and the rapid nucleation and growth of nanoparticles achieved using strategies, such as strong precipitants, high temperatures, and hot injection, contribute to a uniform elemental distribution, disregarding the individual characteristics of the metal precursors [23, 24]. Combining traditional wet chemistry with microwave-assisted synthesis can enhance the overall reaction rate, enabling the successful achievement of the desired goals [25]. In addition to simply increasing the reaction rates, strategies for synthesizing HE-NPs involve using elements with enthalpies near zero [26], the meticulous adjustment of the mixed enthalpies of multiple elements [27], and cation exchange [28].

In wet chemistry synthesis, a wide range of factors, such as the synthesis methods, solvents, precursors, temperature, and ligands, can be extensively controlled to design nanoparticles tailored to target application fields. This is a unique characteristic of wet chemistry synthesis,

which is challenging to achieve with other non-equilibrium synthesis methods, such as carbon arc shock or arc plasma discharge [29–31]. For example, nanoparticles grown in solutions with precise control have been reported, such as 2D high-entropy hydroxides [32], sub-nanometer-sized HEAs [33], and cubic monodisperse high-entropy quantum dots [34]. These examples suggest the potential for the commercialization of high-entropy nanoparticles synthesized using wet chemistry across a wide range of industries, including catalysis, energy storage, sensors, photothermal conversion, and quantum dots.

In this review, we summarize various solution-based synthesis methods for HE-NPs, the strategies and products of each method, as well as explore the types and performance factors of HE-NPs currently being researched in various fields of application.

Fundamental of HE-NPs

Definition of HE-NPs

HE-NPs generally refer to substances in which five or more elements are uniformly mixed to maintain a single-phase solid-solution state. Yeh et al. reported that in an equimolar alloy, at least five elements must exceed 5 at. % and have a configurational entropy change per mole (ΔS_{conf}) of 1.61R or higher to be defined as an HEA [1]. In 2015, Rost et al. reported entropy-stabilized oxides [35], and Sarkar et al. defined a high-entropy oxide (HEO) as a single-phase oxide system containing more than five cations with a value of S_{conf} greater than 1.5R [36].

Recent studies have focused on materials with increasingly complex crystal structures, and the existing approximations of monoatomic gases and Richard's rule are not applicable to ceramic materials [37]. Therefore, an entropy metric (EM) that can be universally applied to crystalline materials is proposed and is defined as follows [38]:

$$\mathrm{EM} = \frac{S^{\mathrm{config}}_{\mathrm{SL/mol\ atoms}}}{R} \times L. \quad (1)$$

Here, $S^{\mathrm{config}}_{\mathrm{SL/\ mol\ atoms}}$ is the configurational entropy calculated using the sublattice model, R is the ideal gas constant, and L is the total number of sublattices. EM values of less than 1, between 1 and 1.5, and greater than 1.5 indicate low-, intermediate-, and high-entropy materials (HEM), respectively. This approach has been successfully applied to HE-NPs (Fig. 1a) [38].

Thermodynamic Insights into the Fabrication of HE-NPs

Considering thermodynamics, the Gibbs free energy ($\Delta G_{mix} = \Delta H - T^{*}\Delta S_{mix}$) of these HE-NPs is influenced by both entropy and enthalpy. Therefore, a thorough understanding of the enthalpy, in addition to the previously discussed entropy, is essential for the fabrication of HE-NPs. A high entropy acts as a driving force for the uniform mixing of elements into a single-phase particle, and increasing the number of constituent elements or synthesis temperature can increase ΔS_{conf} (Fig. 1b) [26]. Moreover, the mixing enthalpy (ΔH_{ij}) is determined by the synergy of various elements with different enthalpies. If ΔH_{ij} is positive under equilibrium conditions such as in wet-chemical processes, it induces phase separation into immiscible phases, whereas negative ΔH_{ij} values and the oxidation potential promote structural ordering such as intermetallic formation. Conversely, when ΔH_{ij} approaches zero, indicating minimal interatomic attractions and repulsions, a uniform high-entropy single phase is formed (Fig. 1c) [26, 27, 39].

Solution-Based Synthesis Methods for HE-NPs

Colloidal Synthesis

Colloidal synthesis is an efficient method for producing a variety of monodisperse NPs with an accurate control over their composition, morphology, and size, and is particularly well suited for creating multi-metallic alloy nanomaterials [46, 47]. According to the La Mer model, the nucleation time plays a vital role in determining the size distribution of the nanoparticles. When the growth rate of the nanoparticles is lower than the nucleation rate, the resulting nanoparticles are smaller, leading to a more uniform distribution (Fig. 2a) [48]. During the synthesis process, precursors are reduced with the surfactants in an organic solvent (oleylamine, 1-ocatdecene, etc.) under specific temperature conditions (ca.150–350 °C) [49]. Surface ligands are employed to control the morphology and size of nanoparticles and prevent their aggregation, thereby stabilizing their growth via the formation of ionic or covalent bonds on their surfaces [50, 51]. These methods can be broadly divided into one-pot and injection processes.

One-Pot Method

The one-pot process, also known as heat-up procedure, begins by introducing precursors, ligands, and solvents at the outset of the reaction. Despite slight heterogeneities during the process, initially forming one or two different metal

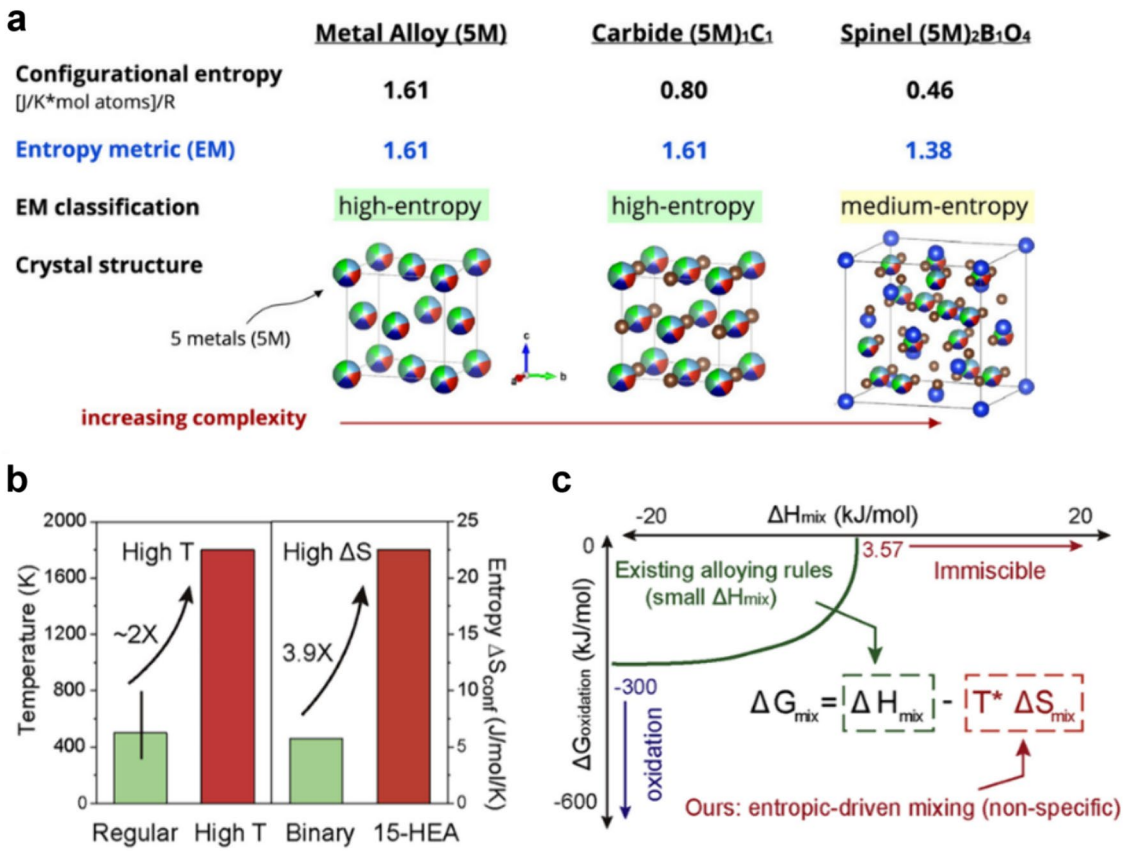

Fig. 1 **a** Configurational entropy, entropy metric, EM classification, and structural information for each crystal. Reprinted with permission from Elsevier [38]. **b** Entropic driving force of a high temperature and high entropy compared with typical nanomaterial studies. Reprinted with permission from Elsevier [26]. **c** Strategies for high-entropy alloys based on the entropic contribution ($-T\Delta S_{mix}$). Reprinted with permission from Elsevier [26]

precursors followed by the incorporation of others, this method remains straightforward and time efficient [47, 52]. HE-NPs synthesized using one-pot methods exhibit various structures (nanoplates [53], nanowires [54], cubes [55], etc.), with the spherical structure being the most representative. Li et al. synthesized spherical uniform $Pt_{18}Ni_{26}Fe_{15}Co_{14}Cu_{27}$ NPs with a size of 3.4 ± 0.6 nm using this facile method [56]. Another notable example is demonstrated by Wen et al., who produced PtRhBiSnSb high-entropy intermetallic (HEI) nanoplates with a hexagonal close-packed (hcp) crystalline structure [41]. Their method initiates with the formation of a Bi complex that serves as a template for nanoplate growth, followed by the subsequent sealing of Pt and Sn. Rh and Sb metals are then seamlessly integrated, diffused, and arranged, resulting in the uniform production of (PtRh)(BiSnSb) HEI nanoplates with an average edge length of approximately 6.2 nm (Fig. 2b). Furthermore, Chen et al. synthesized $Pt_{34}Fe_5Ni_{20}Cu_{31}Mo_9Ru$ HEAs with convex cubic shapes (Fig. 2c) [42]. The key factor is that the shape changes depending on the presence or absence of Ru. Despite using a small amount of Ru (approximately 1%), the shape evidently transitions from a simple cube to a convex cube. Consequently, the pointed pyramids on the convex cubic HEAs (Fig. 2d), with a diagonal length of approximately 38.5 nm, exhibited a high ratio of under-coordinated atoms, leading to enhanced catalytic performance. In this manner, the one-pot approach facilitates the fabrication of various HEAs.

Additionally, HEOs possess autonomous anion–cation sublattices, which demonstrate elevated configurational entropy, resulting in increased lattice distortion and improved durability**.** For example, Sun et al. synthesized CuCoFeNiMn–CeO_2 [57]; this oxide demonstrated a truncated octahedral morphology with dimensions of 5 nm, and a fluorite lattice crystal structure, which is recognized as one of the most stable structures in CeO_2. At this point, a transition metal significantly smaller than Ce is introduced, leading to a size disparity that induces local distortion, consequently yielding short-range nonperiodic characteristics. Consequently, this results in structural heterogeneity via the formation of an oxide–oxide interface, which is stabilized by the entropy. Moreover, an increase in the transition

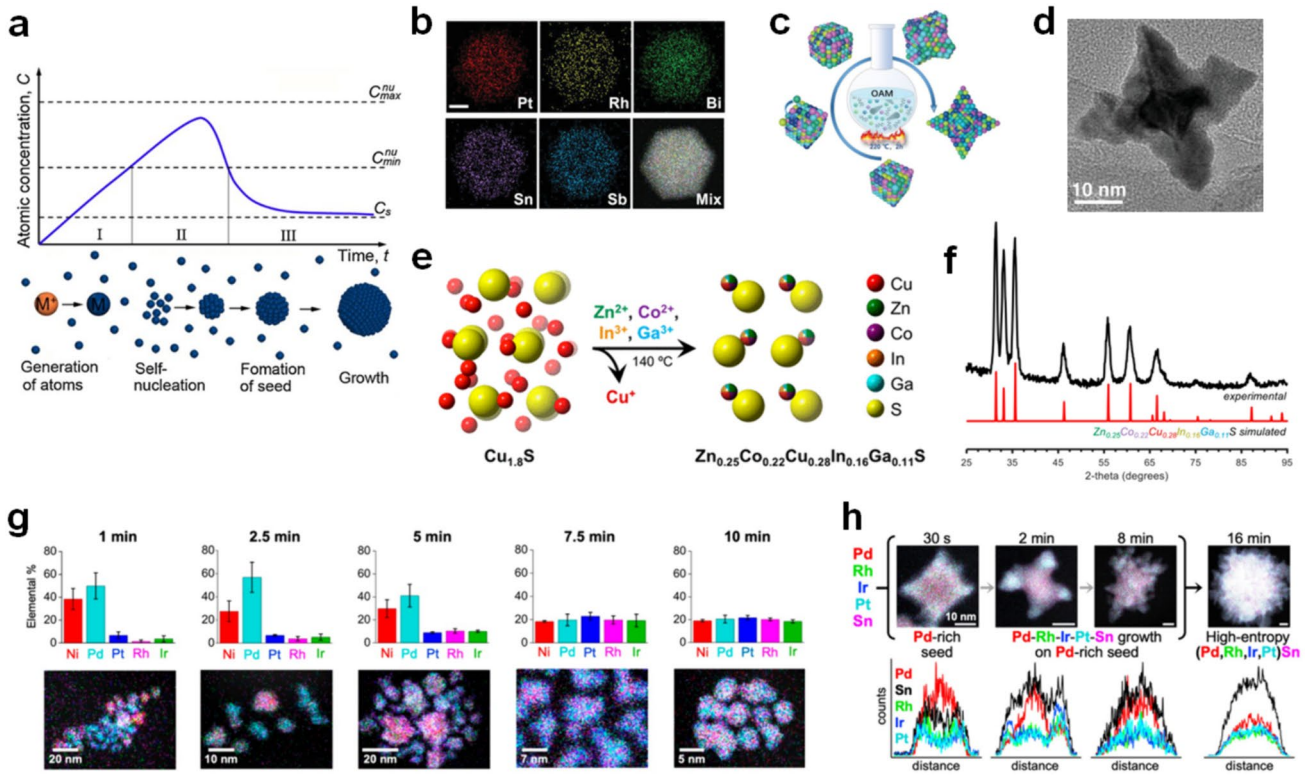

Fig. 2 **a** Nucleation and growth process in the production of uniform NCs within the framework of the La Mer model. Reprinted with permission from Elsevier [40]. **b** EDX mapping visuals depicting a nanoplate composed of PtRhBiSnSb HEI. Scale bar: 5 nm. Reprinted with permission from John Wiley and Sons [41]. **c** Schematic diagram of the synthesis of $Pt_{34}Fe_5Ni_{20}Cu_{31}Mo_9Ru$ HEAs. Reprinted with permission from John Wiley and Sons [42]. **d** High-magnification TEM image of $Pt_{34}Fe_5Ni_{20}Cu_{31}Mo_9Ru$. Reprinted with permission from John Wiley and Sons [42]. **e** Schematic diagram of the synthesis of $Zn_{0.25}Co_{0.22}Cu_{0.28}In_{0.16}Ga_{0.11}S$. Reprinted with permission from American Chemical Society [43]. **f** Experimental and simulated XRD patterns for wurtzite-type $Zn_{0.25}Co_{0.22}Cu_{0.28}In_{0.16}Ga_{0.11}S$. Reprinted with permission from American Chemical Society [43]. **g** Bar charts and corresponding STEM-EDS element maps illustrating the elemental composition (from EDS measurements) for NiPdPtRhIr nanoparticles isolated at different times during a slow-injection synthesis. Reprinted with permission from American Chemical Society [44]. **h** STEM-EDS element maps for Pd, Rh, Ir, Pt, and Sn were obtained for samples isolated at 30 s, 2, 8, and 16 min during the synthesis of (Pt, Rh, Ir, Pt)Sn nanoparticles, along with a line scan across the particle. Reprinted with permission from American Chemical Society [45]

metal–oxygen shared bonds enhances the generation of surface oxygen vacancies, promoting efficient oxygen activation and replenishment, thereby achieving improved CO oxidation capabilities.

Hot Injection

"Hot injection" is another approach, which involves rapidly injecting a concentrated solution of metal precursors and a reducing agent into a larger volume of hot solvent containing surface-stabilizing agents [49, 58]. Owing to the simultaneous entry of metal salts into the reducing solution, hot injection offers the advantage of controlled reaction rates, allowing a finer control over the resulting shape and size, although it is more complex than the one-pot method. Shi et al. synthesized single-phase $(FeCoNiMoAl)S_x$ via hot injection [11]. First, each metal precursor, along with oleylamine and oleic acid, was added to a flask and mixed for 15 min. Sulfur powder, oleylamine, and oleic acid were thoroughly mixed in another flask. The temperature was then increased to 330 °C, and the solution containing the metal precursor was rapidly injected. This process involves a higher temperature for the reaction than that of the thermal decomposition of metal acetylacetonate to break the bond between the metal and oxygen (M–O) and obtain metal sulfide. Subsequently, the mixture was stirred at 330 °C for 30 min to obtain a black colloidal solution. The particles obtained using this technique were enclosed within micelles. Consequently, ligand exchange was performed using $NOBF_4$ to treat the catalyst surface. The resulting $(FeCoNiMoAl)S_x$ had a spherical structure with sizes ranging from 10 to 12 nm. This nanostructure exhibits a high surface area, leading to an improved electrochemical performance. Moreover, its hexagonal sulfide crystal structure is stable in oxidizing environments and acts as a transition metal intermediate, thus offering stabilization advantages.

McCormick et al. introduced a simultaneous multication exchange method for synthesizing metal sulfides ($Zn_{0.25}Co_{0.22}Cu_{0.28}In_{0.16}Ga_{0.11}S$) via hot injection at low temperatures (Fig. 2e) [43]. Initially, four metal precursors ($ZnCl_2$, $CoCl_2$, $InCl_3$, and $GaCl_3$) were dissolved in oleylamine, octadecene, and benzyl ether, followed by Ar purging. The solution was stirred at 180 °C for 30 min and then cooled to 140 °C. Subsequently, a solution of the $Cu_{1.8}S$ nanospheres in Trioctylphosphine (TOP) was rapidly injected into the solution, and the temperature was raised once again to 180 °C for 15 min of stirring. In colloidal synthesis, cation exchange occurs sequentially, allowing for a phase distribution. When $Cu_{1.8}S$ is solvated by TOP, it contributes to the enthalpy in the liquid state and facilitates cation exchange with other metal ions in the solution. This exchange allows the entropic release of the Cu^+ ions into the solution, enabling the synthesis of single-phase high-entropy sulfides. Confirmation of the single phase of the synthesized high-entropy sulfide was supported by the XRD patterns (Fig. 2f), which agreed with the experimental and simulated results. The resulting material possessed a wurtzite structure with an average particle size of 13 nm, indicating pristine and undistorted forms of roxbyite.

Slow Injection

Recently, to minimize collisions between atoms of the same element, thereby preventing the formation of isolated metal nanoparticles and promoting the formation of a homogeneous metal alloy, a slow instead of rapid injection was recently introduced. Dey et al. synthesized NiPdPtRhIr, NiFeCoPdPt, SnPdPtRhIr, and NiSnPdPtIr via slow injection [44]. First, each metal salt was dissolved in a small quantity of oleylamine and stirred under a vacuum for 15 min. Octadecene and oleylamine were then stirred at 120 °C for 30 min under an argon atmosphere. Subsequently, the previously prepared metal salt solution was injected into the mixture of octadecene and oleylamine at 275 °C (NiFeCoPdPt at 315 °C), at a rate of 0.4 ml/min for 10 min. After the reaction was complete, alloys with spherical structures and crystal lattices were created, each approximately 10 nm in size. This synthesis revealed that slow injection is a useful method for producing homogeneous NPs. To investigate how each metal within the NiPdPtRhIr nanoparticles was uniformly distributed, changes from 1 to 10 min post-injection were observed using a STEM-EDS elemental map (Fig. 2g). Initially, in the Pd-rich Pd–Ni seed, other elements began to be incorporated after 7.5 min, leading to a more even distribution. These observations contributed to our understanding of the production of HEA-NPs from metal precursors. As another example, Soliman et al. synthesized (Pd, Rh, Ir, Pt) Sn nanoparticles in the same manner as previously described, using slow injection at a rate of 0.25 ml/min for 16 min [45]. By controlling the rapid reduction of Pd and Pt salts via a slower injection compared to the previous method, they were able to synthesize a more uniform high-entropy alloy. Similar to the study by Dey et al., note that the morphology evolves with changes in the composition, depending on the quenching time after injection (Fig. 2h). Initially, a cube-like structure with a composition of $Pd_{0.29}Rh_{0.21}Ir_{0.05}Pt_{0.14}Sn_{0.31}$ is demonstrated, which is rich in Pd and Sn. Note, most of the Pd is concentrated in the central area, whereas the other metals are predominantly located at the corners. Over 16 min, the metals gradually adopted a flower-like morphology, integrating as they diffused from the corners to the center, ultimately resulting in the synthesis of a high-entropy alloy with a uniform nanoflower morphology.

Based on previous experimental results, the colloidal method is relatively simple and cost-effective compared to other synthetic methods for synthesizing HE-NPs and can control the shape and size. It is believed that it might be more helpful studying the synthesis mechanism of HE-NPs by understanding the process of integration.

Solvothermal Synthesis

Solvothermal synthesis is a straightforward approach used to synthesize nanoparticles, such as metal alloys, spinel oxides, and perovskite oxides in polar solutions. This method enables the formation of various crystal lattices and elemental combinations depending on the type of solvent used, making it particularly effective for producing uniform crystalline nanoparticles at relatively low temperatures [65–67]. The conventional solvothermal synthesis process involves placing a solution containing precursor nitrates or chlorides, pH adjusters, and capping agents in an autoclave and maintaining it at 120–240 °C for a specific period to induce nucleation and particle growth (Fig. 3a) [59, 68]. Compared to other methods used for synthesizing HE-NPs, such as thermal shock, plasma, and colloidal methods, solvothermal synthesis proceeds at relatively low temperatures, requiring several hours to more than a day for nucleation and growth [69].

Depending on the synthesis conditions, including the time, solvent, precursor, pH, stabilizer, and capping agent, a wide range of nanoparticles, ranging from a few nanometers to several tens of micrometers in size can be synthesized. In addition, unlike colloidal synthesis, which is sensitive to moisture, synthesis under solvothermal conditions is less sensitive to the moisture content of the precursor, making the experimental conditions less harsh [70, 71].

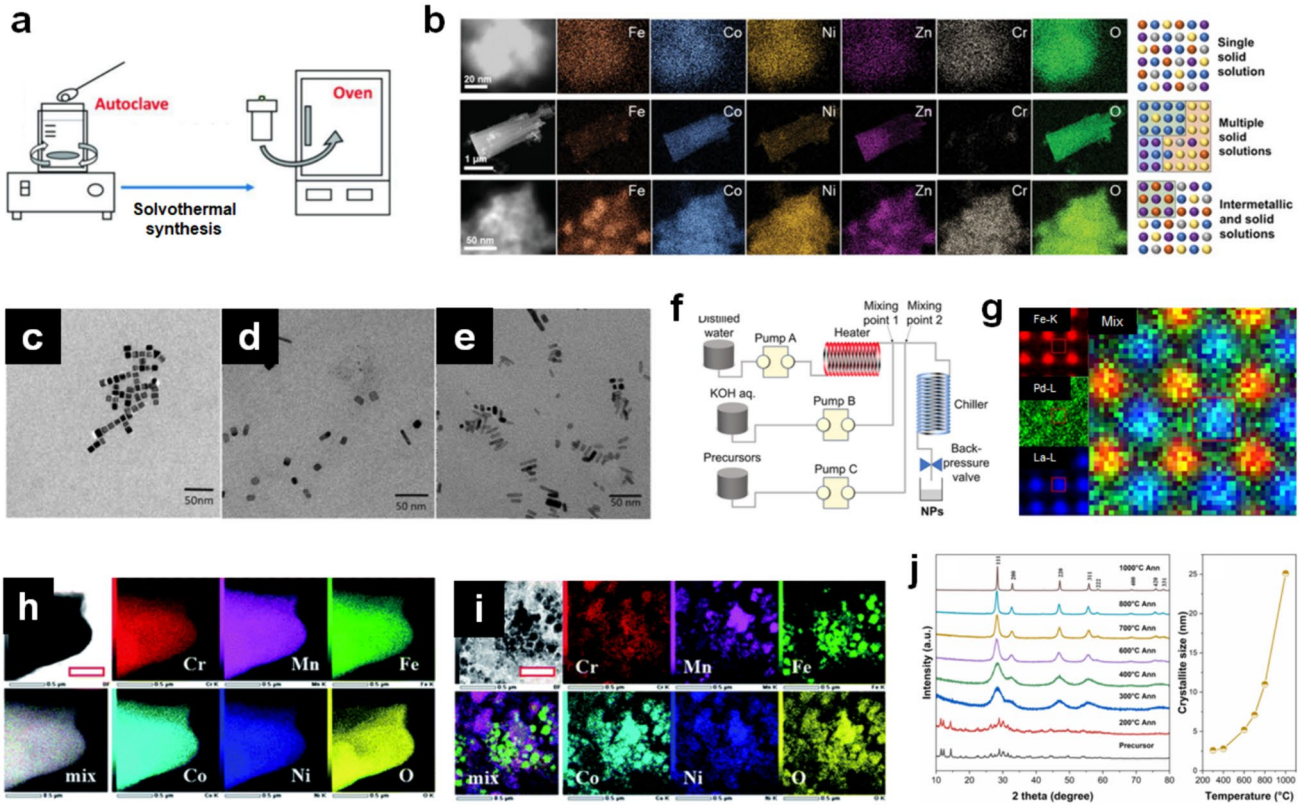

Fig. 3 **a** Schematic of the solvothermal synthesis [59]. **b** EDS images and schematics of the nanoparticles, each containing single, multiple, and intermetallic solid solutions. Reprinted with permission from John Wiley and Sons [60]. TEM image of nanoparticles synthesized by adjusting the volume percent of ethylene glycol to **c** 10% (V/V), **d** 50% (V/V), and **e** 90% (V/V). Reprinted with permission from Elsevier [61]. **f** Diagram illustrating the flow reactor setup. Reprinted with permission from American Chemical Society [62]. **g** Corresponding EDS maps for Fe, Pd, and La. Reprinted with permission from American Chemical Society [62]. NPs synthesized via the solvothermal method using **h** ethylene glycol and **i** DI water under the same conditions [63]. **j** XRD patterns and crystallite size as a function of the annealing temperature. Reprinted with permission from Elsevier [64]

Synthesis of HE-NPs Using the Hydrothermal Method

Hydrothermal synthesis involves creating a high-temperature and high-pressure environment using water-containing metal salts, leading to the hydrolysis of metal salts or precursors to form metal hydroxides, which then aggregate to form fine particles [72]. HE-NPs can also be synthesized by this process; for example, Nguyen et al. prepared high-entropy spinel oxide with a uniform elemental distribution by maintaining a solution containing DI water, (1-hexadecyl) trimethylammonium bromide (CTAB), and urea at 140 °C for 5 h [73]. Although the successful synthesis of HE-NPs via hydrothermal methods is possible, phase segregation or elemental agglomeration may occur within the particles (Fig. 3b), owing to the slower reaction kinetics in hydrothermal processes compared to co-precipitation, where nucleation and particle growth rapidly occur.

The precipitation of metal ions in a solution involves the pK_{sp}. During rapid synthesis processes such as co-precipitation, different elements with distinct pK_{sp} values can reach a state of supersaturation and form a single solid solution. However, slow particle growth in hydrothermal methods increases the possibility of phase segregation owing to the disparate pK_{sp} values of the elements in the solvent [74]. For example, metal ions with larger pK_{sp} values, such as Fe^{3+} and Cr^{3+}, may precipitate first, hindering the formation of a single solid solution of nanoparticles synthesized via hydrothermal methods [60].

To address these issues and optimize the viscosity, solubility, and reactivity of the synthesis solvent for producing high-quality HE-NPs, various solvents are occasionally mixed with water. A notable example is the polyol-hydrothermal method, which involves mixing water with ethylene glycol. Wang et al. conducted a study in which a solution containing ethylene glycol (EG), ethanol, deionized water, and metal nitrate precursors was treated at 180 °C for 24 h to produce $(CoCrFeNiAl)_3O_4$ nanoparticles with a spinel-phase [75]. Similarly, Wu et al. added poly(N-vinyl-2-pyrrolidone) (PVP) as a protective agent to a solution of triethylene glycol and deionized water, followed by heating it to synthesize

IrPdPtRhRu HEA-NPs; this nanoalloy had an average diameter of 5.5 ± 1.2 nm and exhibited a uniform elemental distribution [76].

When utilizing the polyol-hydrothermal method, the water-to-EG ratio and presence of stabilizers such as PVP significantly influenced the monodispersity and size of the resulting nanoparticles. For the synthesis of Pd nanoparticles, PVP acted as a stabilizer, preventing the nanoparticles from agglomerating, whereas the Br^- ions from KBr acted as capping agents, promoting the development of specific facets and inducing square-shaped nanoparticles. Modifying the water-to-EG ratio also allowed controlling the shape of the synthesized nanoparticles. When the volume ratio of EG was high, the reduction of Pd occurred more rapidly, resulting in the formation of nanorod-shaped particles; conversely, when the volume ratio of EG was low, square-shaped particles formed (Fig. 3c–e) [61]. These methods for controlling the nanoparticle morphology are expected to be extended to the fabrication of HE-NPs.

Continuous hydrothermal synthesis is a recent advanced method, which involves the rapid synthesis of nanoparticles by allowing water, which is adjusted to a supercritical state (374.2 °C, above 217.6 atm), to flow through narrow channels encountering precursors along the way (Fig. 3f). In this process, water transitions into a non-polar solvent as its dielectric constant decreases from 80 to less than 10 in the supercritical state. Additionally, the ionization of oxygen and hydrogen in the supercritical water facilitates chemical reactions.

For example, Hanabata et al. utilized a supercritical hydrothermal flow-synthesis method, operating at 450 °C and 30 MPa, to instantaneously react a supercritical solution containing KOH and precursors for producing high-entropy perovskite nanoparticles that incorporated ten different types of cations. The resulting nanoparticles exhibited a uniform distribution of cations, with La, Ca, Sr, and Ba occupying the A sites, and Mn, Co, Ru, and Ir evenly distributed across the B sites of the perovskite structure. Note that Pd was distributed at both the A and B sites (Fig. 3g) [62].

Synthesis of HE-NPs via the Non-hydro Solvothermal Method

In solvothermal synthesis, which does not utilize water, the polyol process is the most commonly employed method. The polyol process involves dissolving metal precursors in a glycol solvent, heating the solution to the reflux temperature, and maintaining the temperature for a certain period. The use of ethylene glycol as a solvent reportedly enhances the ion reduction rates, thereby contributing to a more uniform elemental distribution in materials composed of multiple cations.

Li et al. synthesized high-entropy transition-metal (Co, Cr, Fe, Mn, Ni, and Zn) hydroxides using ethylene glycol and DI water as solvents. The particles synthesized using ethylene glycol as the solvent exhibited a more uniform elemental distribution and larger particle sizes than those synthesized under the same conditions using DI water (Fig. 3h, i). Furthermore, researchers have manipulated the morphology of the synthesized materials by adjusting the pH of the solvent and transforming the spherical clusters into 2D layered sheets, which demonstrated a higher elemental homogeneity than other materials synthesized using ethylene glycol as a solvent [63]. Additionally, the production of lanthanide oxide nanoparticles, specifically $(La_{0.2}Y_{0.2}Nd_{0.2}Sm_{0.2}Gd_{0.2})_2Ce_2O_{7-\delta}$, via the polyol process was reported. Annealing the synthesized nanoparticles at temperatures ranging from 200 to 1000 °C resulted in an increased crystallinity and crystallite size at higher annealing temperatures (Fig. 3j) [64].

In addition to the polyol process, using a solvent mixture containing isopropanol and glycerol for the solvothermal synthesis is promising. When nitrate precursors are used, spherical high-entropy glycerates ranging from hundreds of nanometers to several micrometers in size are synthesized [77, 78], which can be further transformed into high-entropy sulfides by mixing with thioacetamide and ethanol and maintaining the mixture at approximately 160 °C. Acetone and toluene, which have a high solubility for acetylacetonate precursors, can be utilized for producing metal alloys [79, 80]. Bondesgaard et al. prepared RuPtRhPdIr metal alloy nanoparticles by dissolving (Ru, Pt, Rh, Pd, and Ir) acetylacetonate precursors in a solvent composed of acetone and ethanol at a 1:1 ratio and maintaining the solution at 200 °C [81].

Co-precipitation

Co-precipitation synthesis is a cost-effective and straightforward method that rapidly produces particles by mixing precursors and precipitants without the need for complex auxiliary synthesis equipment. Particularly, for the manufacturing of HE-NPs, the rapid reduction of metal ions can contribute to a uniform elemental distribution in the final particles by disregarding the differing precipitation rates of individual metals. The basic sequence for obtaining particles via co-precipitation is as follows: (1) dissolution of the precursor and precipitant, (2) precipitation reaction via mixing, (3) particle separation, (4) washing, and (5) obtaining the precipitate after drying. Thus, co-precipitation synthesis is environmental-friendly and suitable for large-scale industrial processes when compared to other synthesis methods [89–91].

Depending on the order of adding the precursor and precipitant, co-precipitation can be classified into forward or reverse co-precipitation. Forward co-precipitation involves

adding a precipitant to the precursor solution, whereas reverse co-precipitation involves adding the precursor solution to the precipitant solution (Fig. 4a) [82]. These differences in the sequence can lead to variations in the yield, morphology, and properties of the final product, and thus, it must be considered for nanoparticle synthesis via co-precipitation [92].

Furthermore, when combining the precursor and precipitant solutions, adding them simultaneously or dropwise can also lead to differences in the resulting product. The solutions are typically added simultaneously when nanoparticle formation occurs slowly over several hours. Conversely, if an immediate reaction occurs between the precursor and precipitant, slowly mixing the solutions dropwise is advantageous for producing high-quality nanoparticles.

High-entropy hydroxide (HEH) is primarily synthesized via co-precipitation using nitrate or chloride precursor solutions, along with NaOH or ammonia precipitants. Talluri et al. synthesized CrMnFeCoNi HEH using ammonia as a precipitant. These HEH materials can be subsequently utilized as precursors by undergoing high-temperature calcination to crystallize into spinel-structured HEO, similar to the sol–gel method [93]. The synthesis of high-entropy hydrotalcite nanosheets containing up to nine different cations using NaOH as a precipitant has also been reported [60]. Additionally, Okejiri et al. synthesized spherical perovskites, such as BaSr(ZrHfTi)O_3, BaSrBi(ZrHfTiFe)O_3, and Ru/BaSrBi(ZrHfTiFe)O_3 nanoparticles by ultrasonicating a solution containing a NaOH precipitant and precursors (Fig. 4b) [83].

Although annealing can convert HEH to HEO, methods for directly synthesizing HEO have been reported. Rong et al. produced IrRuCrFeCoNiO_x nanoparticles by precipitating a precursor with sodium carbonate in one step. The synthesis process involved adding a sodium carbonate solution to the precursor solution dropwise. The synthesized nanoparticles exhibited agglomerated small particles, and unlike the HEO produced via annealing, it demonstrated the complete lack of or weak peaks of amorphous phases in the XRD analysis (Fig. 4c) [84].

In addition to HEO- or HEH-series nanoparticles, various types of HE-NPs can be synthesized via co-precipitation. For example, Gao et al. prepared CoNiMnCuFeMgZnSr HE ammonium phosphate using NH_4Cl and $(NH_4)_3PO_4{\cdot}3H_2O$ precipitants. The synthesized nanoparticles exhibited a flower-like morphology, comprising elongated disk-shaped particles with a uniform elemental distribution ranging from 6 to 10 µm in diameter (Fig. 4d) [85]. An elongated disk shape was predominantly observed when cobalt phosphate was synthesized via co-precipitation. Research regarding HE-NPs utilizing rare-earth elements has also been conducted. Shen et al. fabricated uniform nanocubic high-entropy Prussian blue analogue $Mn_{0.4}Co_{0.4}Ni_{0.4}Cu_{0.4}Zn_{0.4}[Fe(CN)_6]_2$ composites using a $K_3[Fe(CN)_6]$ precipitant [94]. Additionally, the synthesis of HE rare-earth monosilicates and disilicates using rare-earth oxide precursors, HNO_3, and ammonia precipitants has been reported [95].

Pulsed Laser/Laser Scanning Ablation in Liquid

Pulsed laser ablation in liquid (PLAL) is used to obtain stable HEA-NPs without using a ligand [96]. While the initial purchase of a laser generation device may incur costs, this synthetic approach is facile, simple, and reproducible. It has the advantage of synthesizing combinations of multiple elements regardless of their thermodynamic solubility. Additionally, this method is relatively environmentally friendly compared to other synthesis techniques, such as colloidal synthesis, which often involve the use of toxic organic chemicals, as it requires minimal additional chemicals beyond the solution and precursor [96, 97]. For example, Waag et al. synthesized CoCrFeNiMn HEA-NPs with diameters smaller than 5 nm using picosecond-pulse laser ablation [86]. The synthesis process first exposes the bulk HEAs to a pulsed laser in the liquid, resulting in the formation of a plume owing to mass ionization and atomization within the alloy. Subsequently, the ablated material undergoes nucleation and condensation within the vapor phase of the liquid (Fig. 4e). This synthesis method can rapidly achieve 3 g/h of mass production. Surface segregation was observed, which was attributed to oxidation during the formation of the nanoparticles. Larger nanoparticles have longer residence times in the molten state and interact with oxygen. This process promotes the surface separation of Cr and Mn via selective oxidation.

Johny et al. successfully synthesized CrCoFeNiMn and CrCoFeNiMnMo high-entropy metallic glass NPs with amorphous structures by irradiating an HEA bulk target in acetonitrile [98]. The resulting particles have a slight amount of manganese oxide/hydride to stabilize them within the graphitic shell, and the electrical activity increased owing to the amorphous structure and defects caused by the addition of Mo. Furthermore, in addition to acetonitrile being a solvent, it is also a source of carbon. The formation of C-related compounds stabilizes the amorphous phase and results in a nanoscale size.

In addition to HEAs, high-entropy ceramics can be obtained using laser techniques. Wang et al. fabricated various HEAs and ceramics using laser scanning ablation (LSA) with a pulsed nanosecond laser under mild conditions [99], by which they uniformly synthesized up to nine metals uniformly at significantly high speeds, regardless of their thermodynamic solubility. The particles created using this method exhibited a high performance as bifunctional electrocatalysts.

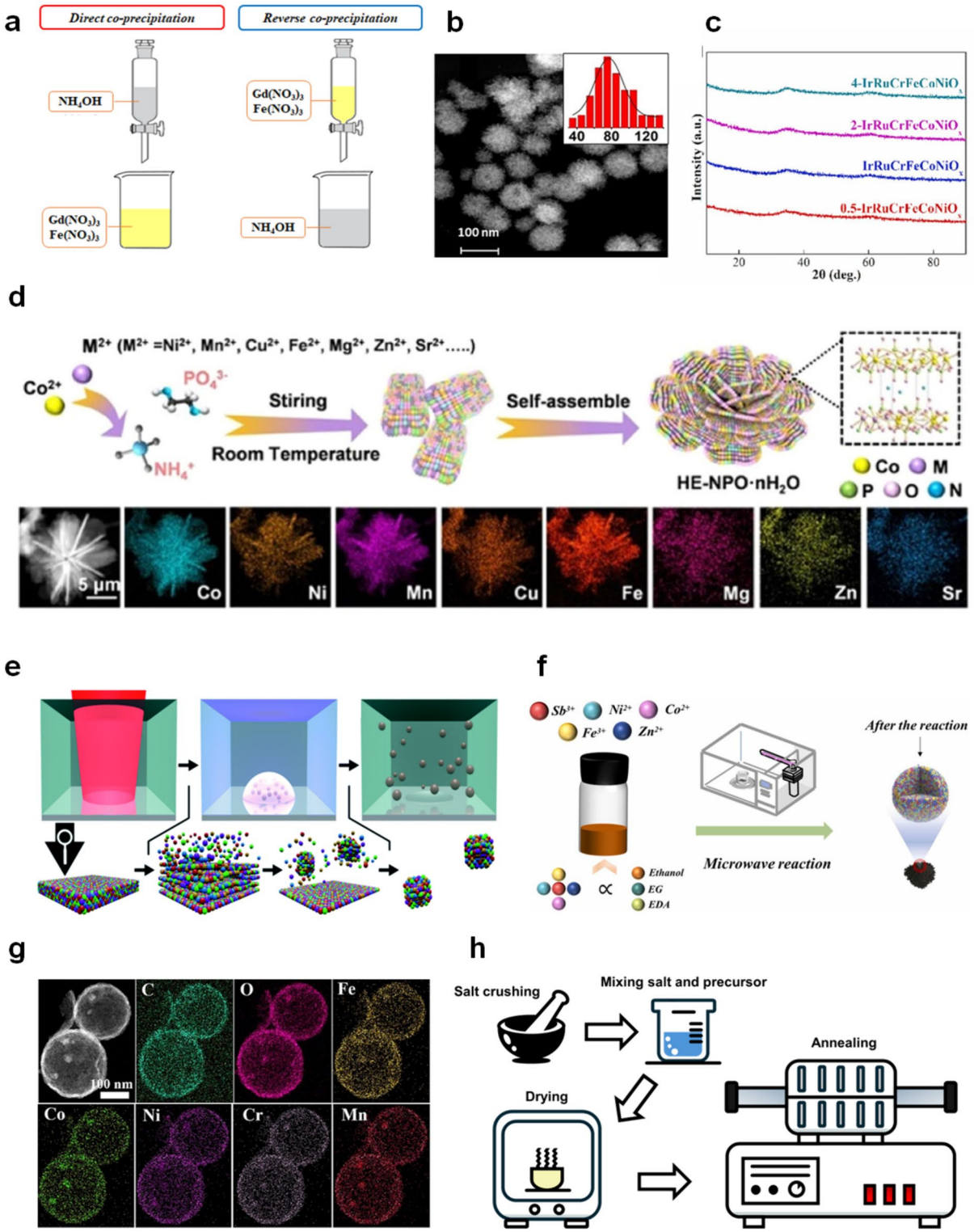

Fig. 4 **a** Schematic of direct and reverse co-precipitation [82]. **b** High-angle annular dark-field (HAADF) images of $BaSr(ZrHfTi)O_3$. Reprinted with permission from John Wiley and Sons [83]. **c** XRD patterns of IrRuCrFeCoNi high-entropy oxides with varying precipitator contents. Reprinted with permission from Elsevier [84]. **d** Synthesis process and EDS images of HE-NPO 3D superstructures. Reprinted with permission from American Chemical Society [85]. **e** Schematic of the laser-based synthesis of CoCrFeNiMn HEA-NPs [86]. **f** Schematic of the microwave-based synthesis method. Reprinted with permission from Elsevier [87]. **g** HAADF-STEM images and EDS maps of hollow mesoporous carbon spheres with nanoparticles. Reprinted with permission from Elsevier [88]. **h** Schematic illustration of the molten salt synthesis process

Microwave Synthesis

The synthesis of HEM using microwaves can be broadly classified into two types. The first type is a high-temperature shock synthesis, which involves microwaves that induce the surface heating of metal powder particles by the induced currents on the surface layers [100].

The second type of synthesis involves irradiating a solution containing the precursors with microwaves to reduce the precursors (Fig. 4f). When microwaves are employed, polar molecules rapidly rotate owing to the oscillation of the electric field, facilitating the collision and heating of the reactants. Additionally, microwaves induce skin effects and the superheating phenomena of the surface in the metal elements within the solution, promoting nucleation and growth, and overcoming the different precipitation rates of metal ions [101, 102].

This approach, which employs polar solvents, is commonly integrated with complementary synthesis techniques such as co-precipitation or solvothermal methods. By blending the hydrothermal method with microwave irradiation, the duration of the reaction is notably reduced to a few minutes, significantly differing from conventional solvothermal processes. Furthermore, this method facilitates prompt nucleation by lowering the reaction temperature, enabling the homogeneous growth of HEM with a uniform elemental distribution [69, 103, 104].

For example, Wang et al. utilized an autoclave coupled with a microwave generator to synthesize $(FeCoNi_2CrMn)_3O_4$ nanoparticles with a spinel structure via a brief 30-min reaction followed by additional annealing. In another study, a solution comprising the precursor, urea, and thioacetamide was heated to 160 °C for 20 min using microwave irradiation, resulting in the synthesis of S-doped HEO, with the doping ratio of S controllable by the amount of thioacetamide [105]. He et al. grew nanoparticles with an average size of 3.3 nm on hollow mesoporous carbon spheres using a similar approach (Fig. 4g) [88].

Microwave-assisted co-precipitation is simpler compared to the preceding method employing autoclaves in conjunction with microwaves for promoting reactions. Kheradmandfard et al. investigated a solution containing a nitrate precursor and NH_4OH precipitant under modified domestic microwave irradiation for 3 min to synthesize single-phase oxides of (Mg, Cu, Ni, Co, Zn)O HEO nanoparticles with an average size of 44 nm [106].

Other Synthesis Methods

In addition to the aforementioned methods, various wet chemistry techniques can be used to synthesize HE-NPs. Several methods that can be used in the experiments are introduced as follows.

Molten Salt Synthesis

The molten-salt method transforms salts from a solid to liquid state at high temperatures, acting as a medium to facilitate stable nanoparticle synthesis at elevated temperatures. When the melting point of a salt is excessively high, two or more salts can be mixed to lower the melting point. For example, when the melting point of NaCl is 800 °C and that of KCl is 775 °C, mixing these salts at a 1:1 ratio forms a eutectic point at approximately 660 °C according to the phase diagram, enabling the synthesis of nanoparticles at lower temperatures [107, 108].

The uniform mixing of the precursors is crucial for producing HE-NPs using the molten-salt method. Several studies have used the method of dissolving precursors in a liquid, followed by drying and then regrinding to achieve uniform mixing [109]. The sequence of processes involved in synthesizing nanoparticles via the molten-salt method, including salt milling, precursor dissolution, drying, and annealing, can be better understood by examining Fig. 4h. The synthesis of HEAs via the molten-salt method has been reported. For example, Kobayashi et al. synthesized AlCoCrFeNiV HEAs using LiCl and $CaCl_2$ salts to reduce the oxide precursors at high temperatures. Although an XRD analysis did not detect oxide phases in the synthesized particles, EDS revealed the formation of small oxide layers on the surface [110]. Studies regarding the synthesis of various types of HE-NPs, including oxides [111], carbides [112, 113], and borides [114, 115], via molten-salt synthesis have been reported, with varying results depending on the type of salt, synthesis conditions, and additives used.

High-Temperature Liquid Shock Synthesis

Thermal shock methods typically involve immersing materials such as carbon fibers into a liquid precursor, followed by drying and exposure to high temperatures. This approach is useful for fixing high-entropy phases in nanoparticles through the generation and rapid cooling of nanoparticles at high temperatures. However, it has drawbacks, such as uneven particle-size distribution and potential substrate damage due to instantaneous high temperatures, making it challenging to deposit nanoparticles on substrates like metal foam or thin foil [6, 116].

Cui et al. adopted an innovative approach to synthesize HEAs using a high-temperature liquid shock method. In this method, carbon fibers immersed in a solution are instantaneously subjected to high temperatures by passing a current through them. This technique can overcome the aforementioned issues, providing a more uniform

particle-size distribution and reducing substrate damage. Specifically, the synthesis involved immersing the carbon fiber felts in a mixture of oleylamine, oleic acid, formaldehyde solution, carbon black, and metal precursors under an Ar atmosphere with a current of 38 A applied for 60 s. Consequently, PtCoNiRuIr/C HEAs with a mean diameter of 3.24 nm were obtained, demonstrating a uniform elemental distribution. During particle formation, oleylamine and oleic acid served as dispersants and blocked mass transfer to the nanoparticles. Thus, the solvent functioned as a ligand, resulting in smaller and more uniformly distributed nanoparticles attached to the carbon fiber surface compared to the traditional carbon thermal shock synthesis, thereby suppressing aggregation [117].

Liquid Metal Synthesis

In 2023, Cao et al. reported the first synthesis of HEAs using liquid metals, for which they first produced Ga, In, and Sn nanoparticles using ultrasonic treatment. The synthesized nanoparticles were then mixed with various metal salts to prepare the precursor, which was heated to 923 K in an Ar/H_2 atmosphere to synthesize the HEAs. During the synthesis, the oxide coating surrounding Ga, In, and Sn at high temperatures was destroyed owing to the thermal expansion difference compared to the inner metals, ensuring fluidity. In addition, the low melting points of liquid metals provide a stable liquid environment for homogeneous elemental mixing. Among the Ga, In, and Sn used in the experiment, the HEAs synthesized using Ga exhibited the highest elemental uniformity, because Ga has a relatively negative enthalpy, which reduces its Gibbs free energy and overcomes the immiscibility of the alloy system [118].

Applications

We explored the synthesis of HE-NPs using wet-chemical methods in the preceding sections. HE-NPs are currently being evaluated as promising materials for various engineering applications owing to their unique physicochemical properties, which have been reported in an increasing number of related studies. Therefore, the effective utilization of HE-NPs in each application area and the approaches that should be adopted for their synthesis are assessed herein. This classification will contribute to reducing trial and errors for the study of HE-NPs conducted by numerous researchers in the future [116, 119].

Water Electrolysis Catalyst

Research regarding high-entropy water-electrolysis catalysts is being conducted to overcome the overpotential limitations of conventional electrolysis catalysts. HE-NPs catalysts synthesized using various methods have demonstrated excellent performances in electrolysis reactions. Most of the HEA catalysts reported in these studies exhibited higher turnover frequency (TOF) values than those of commercial Pt/C and Ru/C catalysts. TOF is typically explained by the hydrogen adsorption energy associated with the d-band center; however, HE-NPs have a broader distribution of d-band centers owing to their atomic arrangements on the surface that are more complex. This extension of the d-band center distribution can result in unique activities that cannot be solely explained by the hydrogen adsorption energy. Additionally, HE-NPs exhibit solid-solution strengthening and sluggish atomic diffusion effects owing to their high entropy, which contribute to the overall stability of the catalytic reactions of HE-NPs [124, 125].

Acidic HER Catalyst

Various methods are available for synthesizing HEA catalysts for the acidic hydrogen evolution reaction (HER). Feng et al. dissolved sulfate-series precursors in a 0.002 M H_2SO_4 solution, followed by the addition of sodium borohydride and carbon powder to obtain a precipitate. Carbon-supported ultrasmall high-entropy alloy (us-HEA) was then prepared via annealing in H_2/Ar at 350 °C, which being composed of NiCoFePtRh, achieved a high mass activity of 28.3 A mg^{-1} noble metals at − 0.05 V (vs the reversible hydrogen electrode, RHE) for the HER in a 0.5 M H_2SO_4 solution, demonstrating to be 40.4 times higher than that of commercial Pt/C. Additionally, us-HEA/C exhibited a significantly high TOF (30.1 s^{-1}) at a 50-mV overpotential and demonstrated no significant performance degradation despite following 10,000 cycles. The Pt sites on the us-HEA (111) surface exhibited an excellent activity during the Tafel step, whereas Rh played a crucial role in the Volmer step. The Fe/Co/Ni atoms primarily regulated the electronic structure of the Pt/Rh atoms and increased the entropy of the us-HEA, enhancing its stability. The synergy among these five elements in the us-HEA resulted in its high HER performance [126].

Minamihara et al. synthesized IrPdPtRhRu HEA-NPs using a continuous-flow reactor. The precursor rapidly reacted with a strong reducing agent at room temperature, resulting in the synthesis of extremely small and uniform nanoparticles with an average size of 1.32 ± 0.41 nm. Owing to their high surface-to-volume ratio, these small nanoparticles enable the efficient utilization of precious chemical elements. The synthesized nanoparticles were utilized as HER catalysts and exhibited a significantly low overpotential of

6 mV at 10 mA cm^{-2} in 1 M $HClO_4$, which is one-third that of commercial Pt/C catalysts (Fig. 5a) [120].

Alkaline HER Catalyst

In addition to acidic HERs, noble metal-containing HEA with sub-nanometer diameters also exhibited a high performance in alkaline HER. The colloidal method facilitates the synthesis of well-controlled HEA-NPs with sub-nanometer dimensions, enabling the synthesis of various HEA-NPs, such as Pt(Co/Ni)MoPdRh NPs [127], PtNiFeCoCu NPs [56], and PtRuRhCoNi nanowires [128]. These synthesized HEA-NPs reportedly exhibited overpotentials of approximately 10 mV at 10 mA cm^{-2} in 1 M KOH, achieving a mass activity that was greater than six times higher than that of commercial Pt/C catalysts.

In alkaline HERs without noble metals, high-entropy nitrides [129], phosphides [130, 131], oxides, and chalcogenides [132, 133] have been reportedly used as catalysts. In particular, Chen et al. reported that the $Ni_{30}Co_{30}Fe_{10}Cr_{10}Al_{18}W_2$ HEA doped with P exhibited a low overpotential of 70 mV at 10 mA cm^{-2} in 1 M KOH. Although this overpotential is higher than that of Pt/C (32 mV at 10 mA cm^{-2}), it demonstrated superior performance at high current densities, with an overpotential of 147 mV at 50 mA cm^{-2}, compared to the 228 mV overpotential recorded for Pt/C. The doping of P into the HEA was achieved by annealing a mixture of HEA and NaH_2PO_2 in a N_2 atmosphere at 300 °C. The doping of anions into the HEA resulted in a lattice expansion and surface-lattice strain (Fig. 5b). These surface defects led to the formation of high-energy surface structures that provided a greater number of active absorption sites [121]. Although this material was not produced using wet chemistry, increasing the catalytic activity by enhancing the crystal lattice distortion via anion doping in HEA can be beneficial for the future study of HE-NPs.

Acidic OER Catalyst

The catalysts primarily used for acidic oxygen evolution reactions (OERs) include noble metals such as Ru and Ir. Transition-metal-based catalysts are prone to corrosion in acidic environments, resulting in a lack of transition-metal-based proton-exchange-membrane (PEM) electrolysis cathode catalysts, which are known to offer both a high activity and stability [134]. The characteristics of HE-NPs, including the sluggish diffusion effect and surface-lattice distortion, are promising for utilizing transition-metal elements as PEM electrolysis anode catalysts, providing stability.

Hu et al. synthesized a quinary high-entropy ruthenium iridium-based oxide (M-RuIrFeCoNiO_2) in the form of a

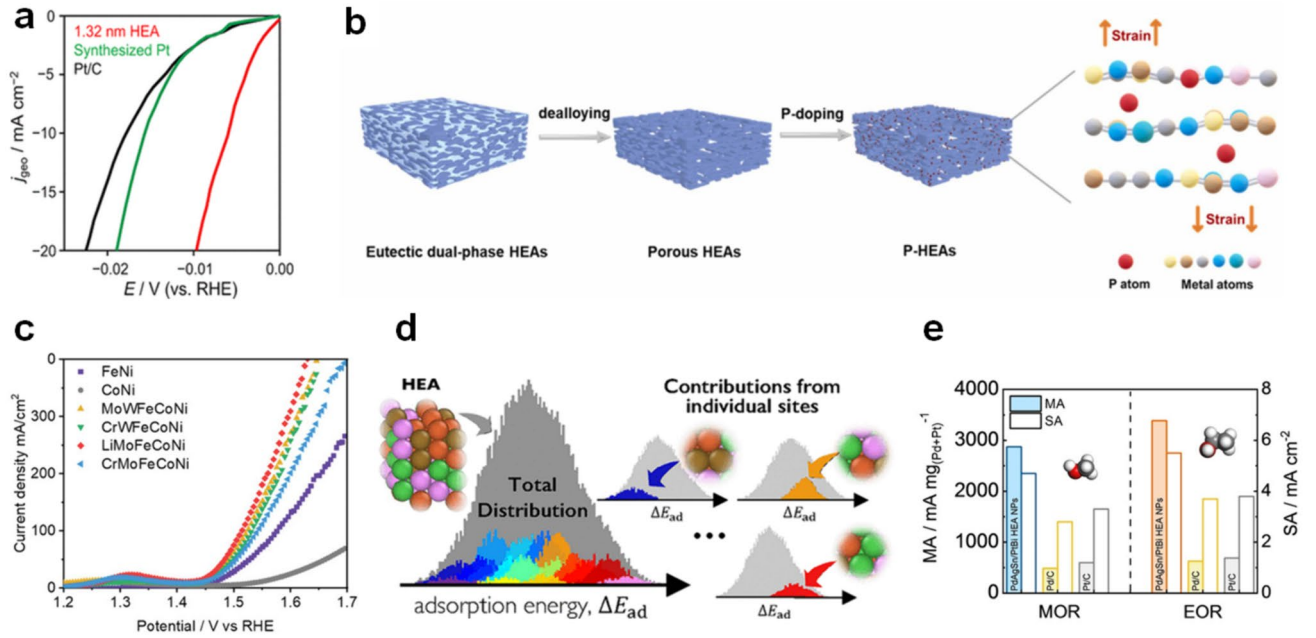

Fig. 5 **a** Polarization curves comparing 1.32 nm HEA-NPs, synthesized Pt NPs, and commercial Pt/C. Reprinted with permission from American Chemical Society [120]. **b** Diagram illustrating the P-HEA synthesis and lattice strain induction. Reprinted with permission from Elsevier [121]. **c** Utilization of HEHs in an electrocatalytic oxygen evolution reaction: LSV curves (5 mV s^{-1}, 90% iR compensation). Reprinted with permission from John Wiley and Sons [60]. **d** Contribution of various elements to the adsorption energy distribution on HEAs. Reprinted with permission from American Chemical Society [122]. **e** Mass activity and specific activity of PdAgSn/PtBi HEAs in MOR and EOR. Reprinted with permission from John Wiley and Sons [123]

nano-sheet with abundant grain boundaries by adding the precursor mixture to molten $NaNO_3$ heated to 350 °C via a molten-salt method followed by rapid cooling. The synthesized catalyst exhibited a low overpotential of 189 mV at 10 mA cm^{-2} for the OER in 0.5 M H_2SO_4, demonstrating significantly improved performance compared to M–RuO_2 (210 mV), C–RuO_2 (253 mV), and C–Ir/C (292 mV). Additionally, it operated for over 500 h without significant performance degradation at a high current density of 1 A cm^{-2}. This superior performance can be attributed to the successful modification of the OER pathway and electronic structure by the transition-metal elements and grain boundaries. Although the transition metals were not utilized as the primary reaction spots, the integration of noble and transition metals in HEM resulted in a better performance compared to single noble metal catalysts, contributing to a reduction in the consumption of expensive noble metals [135].

Alkaline OER Catalyst

In alkaline OERs, high-entropy hydroxides or oxides synthesized via co-precipitation exhibit excellent catalytic performances. Yu et al. prepared 2D high-entropy hydrotalcite nanosheets using the NaOH precipitant at 70 °C. The increase in the reaction temperature and introduction of smaller or larger metal elements into the host lattice during the nanoparticle synthesis process induced lattice distortion on the surface, which contributed to the high catalytic performance. The synthesized LiMoFeCoNi, MoWFeCoNi, and CrWFeCoNi HE hydrotalcites exhibited low overpotentials of 187, 200, and 208 mV, respectively, at a current density of $j = 10$ mA cm^{-2} (Fig. 5c) [60]. Additionally, the amorphous IrRuCrFeCoNiO*x* synthesized using the sodium carbonate precipitant also demonstrated a high performance, with an overpotential of 190 mV at a current density of 10 mA cm^{-2} in 1 M KOH. The extremely disordered atomic arrangement of the amorphous structure and the sub-nanometer thickness of the oxyhydroxides formed on the surface during the OER contributed to the high performance and stability of the OER activity [84].

Complex Chemical Reaction Catalyst

Owing to the lattice distortion caused by the synergy of multiple elements, HE-NPs possess numerous active binding sites. Additionally, the adsorption energy of the HEA can be converted into a continuous spectrum by the synergy of the broadened peaks compared with a single element by electronic hybridization (Fig. 5d). This enables HE-NPs to function as multifunctional catalysts capable of simultaneously adsorbing various intermediates in complex chemical reactions [119, 122].

HEA-NP catalysts that exhibit a high performance in the HER electrode during electrolysis also demonstrate an excellent performance in the oxidation reactions of liquid fuels (methanol, ethanol, glycerol, etc.). In particular, the PtNiFeCoCu NPs catalyst, which is known for its high performance in alkaline HER, exhibited a significantly high mass activity of 15.04 A mg^{-1}_{Pt} in the methanol oxidation reaction under alkaline conditions, demonstrating a good stability with a decrease of only 6.4% in the mass activity after 1000 CV cycles compared to a decrease of 26.9% in that of the Pt/C catalyst [56]. Similarly, the PdAgSn/PtBi HEA-NPs developed by Lao et al. demonstrated a mass activity that was greater than 4.8 times higher than that of the commercial Pt/C and Pd/C catalysts for methanol and ethanol oxidation reactions (Fig. 5e) [123].

Research regarding non-precious-metal-based HEO catalysts have also been reported. Spinel-structured $(CoCrFeMnNi)_3O_4$ HEO NPs synthesized via co-precipitation and annealing exhibited an onset potential of ~ 0.45 V and a mass activity of ~ 110 mA mg^{-1} in the methanol oxidation reaction [136]. Spinel $(Mn,Fe,Co,Ni,Cu)_3O_4$ prepared by using the polyol-hydrothermal method demonstrated an onset overpotential of 0.7 V in the ammonia oxidation reaction, which was ~ 0.2 V lower than that of single-element catalysts [137]. Additionally, perovskite structured HEO NPs composed of ten different cations achieved a CO conversion of 100% at 234℃, whereas $LaFeO_3$ reached the same at 290 °C, demonstrating a high catalytic activity in CO oxidation [62].

Energy Storage

Zinc-air batteries (ZABs) are popular energy storage devices owing to their high-energy capacitance and low contamination [143]; however, challenges such as an inefficient oxygen conversion and instability with the existing alloy catalysts remain. HEA have emerged as a promising solution for creating multiple active sites in oxygen catalysts and potentially enhancing the storage capacity and stability of ZABs. For instance, the He et al. assembled ZABs with CrMnFeCoNi HEA-NPs as the air cathode and Zn foil as the anode (Fig. 6a) [138]. These nanoparticles were synthesized using a solution-based method at a low temperature. The ZAB demonstrated a peak power density of 116.5 mW cm^{-2} and specific capacity of 836 mAh g^{-1} at 8 mA cm^{-2}, which are higher than the 114.1 mW cm^{-2} and 788 mAh g^{-1} of the Pt/C ZAB. The reason for this high performance is that the lattice distortion of the HEA-NPs increases the active electron density around the Fermi level, which accelerates electron movement and lowers the RDS energy barrier, thereby enabling OER and ORR reactions to occur more rapidly. Additionally, Cao et al. developed a multifunctional catalyst, $Fe_{12}Ni_{23}Cr_{10}Co_{30}Mn_{25}$/carbon nanotube (CNT), by

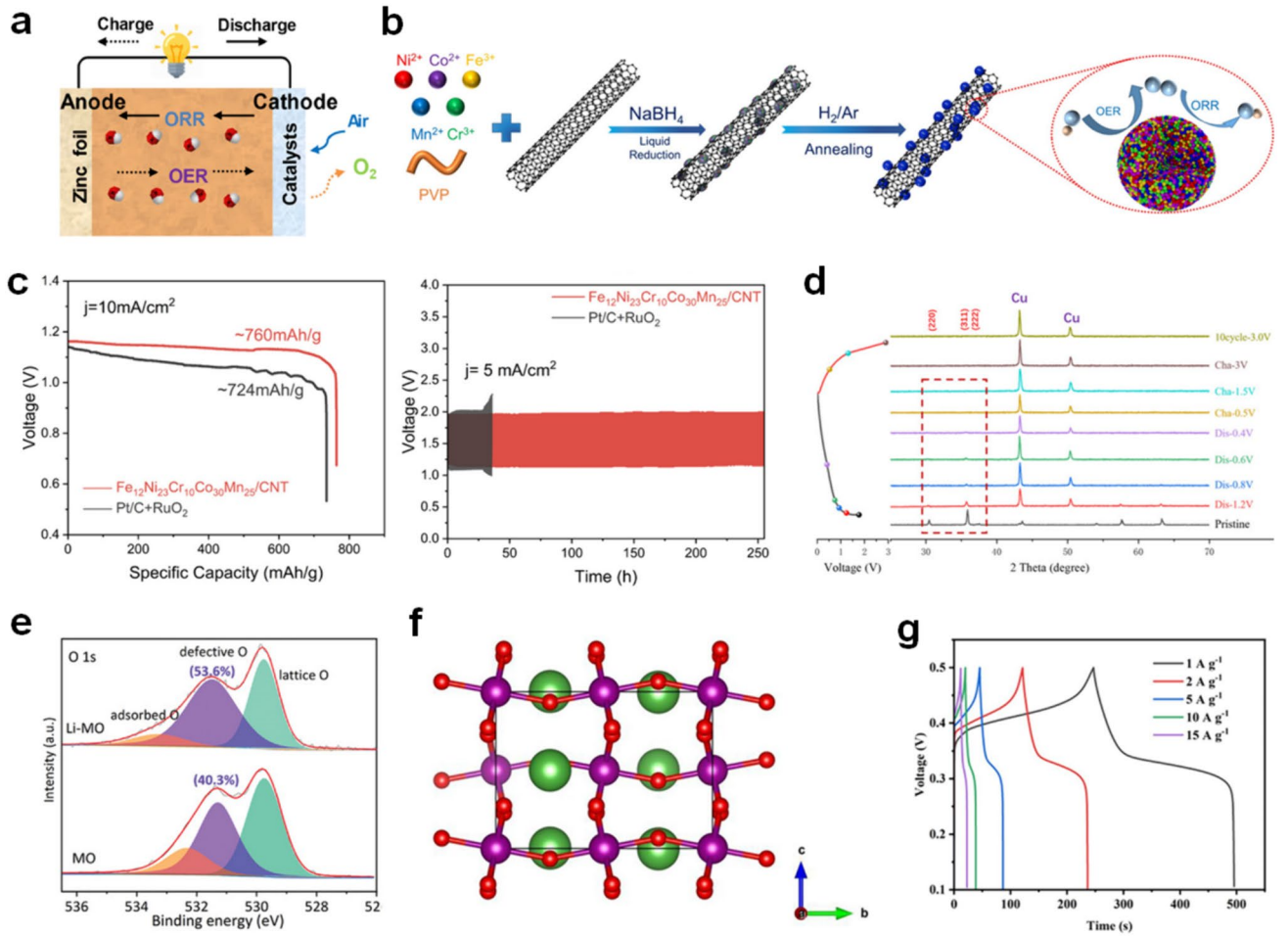

Fig. 6 **a** Schematic diagram of ZAB. Reprinted with permission from Elsevier [138]. **b** Schematic of the bifunctional ORR/OER of $Fe_{12}Ni_{23}Cr_{10}Co_{55}$–$xMn_x$/CNT. Reprinted with permission from American Chemical Society [139]. **c** Specific capacity and long-term cyclic durability of $Ni_{23}Fe_{12}Cr_{10}Co_{30}Mn_{25}$/CNT and Pt/C + RuO_2 from left to right. Reprinted with permission from American Chemical Society [139]. **d** Ex-situ XRD patterns of the HESO electrodes at different charge/discharge potentials. Reprinted with permission from John Wiley and Sons [140]. **e** High-resolution XPS spectra of O 1s in MO and Li-MO. Reprinted with permission from John Wiley and Sons [141]. **f** Schematic illustration of the orthotropic-phase perovskite. Reprinted with permission from Elsevier [142]. **g** GCD curves of $La(Co_{0.2}Mn_{0.2}Fe_{0.2}Ni_{0.2}Cu_{0.2})O_3$. Reprinted with permission from Elsevier [142]

loading HEAs into tubular porous CNT via liquid reduction and annealing (Fig. 6b) [139]. The unique structure of CNTs facilitates both OER and ORR processes by promoting a rapid mass transfer, preventing nanoparticle aggregation, and increasing activity via an increased specific surface area. When employed as an electrode in ZABs, this catalyst achieved a high specific capacity (760 mAh g^{-1}) and energy density (865.5 Wh kg^{-1}) at 10 mA cm^{-2} in an alkaline media, operating for more than 256 h (Fig. 6c).

In addition to ZABs, lithium-ion batteries (LIBs) are well known for their high energy density and rechargeability, which contribute to their relatively long lifespans. HEOs are particularly advantageous as LIB anodes owing to their distinct structural stability and high capacity. An et al. synthesized $(CoMnZnNiMg)_2CrO_4$ using a solution combustion method [140]. In addition to the high-entropy characteristics of this catalyst, an amorphization transformation occurred in the electrode (Fig. 6d), increasing the lithium-ion diffusion coefficient, and ensuring a uniform distribution. This leads to an improved stability and performance of the anode materials. As a result, this material exhibited a remarkable performance (371 mAh g^{-1} at 2000 mA g^{-1}) and stability (608 mAh g^{-1} after 200 cycles at 200 mA g^{-1}). Liu et al. similarly synthesized (LiMgCoNiCuZn)O for LIB anodes using the molten-salt method by introducing Li into (MgCoNiCuZn)O [141]. Introducing Li causes lattice contraction, indicating the presence of an oxygen vacancy (Fig. 6e), as the radius of Li^+ in the six-coordination environment is slightly larger than the average radius of the (MgCoNiCuZn)O. Consequently, the specific capacity reaches 714 mAh g^{-1} at 0.1 A g^{-1}; after 300 cycles, it maintains stable at 417 mAh g^{-1} at 1 A g^{-1}, surpassing the performance of 5-cation oxides.

Similar to batteries, supercapacitors are recognized as advantageous energy storage devices owing to their higher power density, cycling stability, reversibility, rapid charge–discharge rates, wide operating temperature range, and other beneficial characteristics [144]. Meng et al. fabricated $La(Co_{0.2}Mn_{0.2}Fe_{0.2}Ni_{0.2}Cu_{0.2})O_3$, which is classified as a hollow spherical multilayer structure of high-entropy perovskite oxides (HSM-HEPs), using acidic carbon spheres as synthetic templates in the liquid phase [142]. This fabrication method resulted in a single-phase HEP with orthorhombic structures (Fig. 6f), abundant oxygen vacancies, and multiple layers, leading to a large specific surface area and high specific capacity. When employed as electrodes for supercapacitors, they exhibited a specific capacitance of 625F g^{-1} at 1 A g^{-1} (Fig. 6g), maintaining a capacitance retention of 88% despite following 10,000 cycles.

Sensor

Chemiresistive Sensors

The effective detection of major greenhouse gases (CO_2, CH_4, etc.) is not only environmentally important, but also essential for a safe working environment and health. Compared with the existing metal-based oxide sensors, HEO sensors have advantages such as a low power consumption and operation at room temperature, making them more conducive to commercialization. Naganaboina et al. developed $Gd_{0.2}La_{0.2}Y_{0.2}Hf_{0.2}Zr_{0.2}O_2$(Y-HEC) NPs as CO_2 sensors [145]. $Gd_{0.2}La_{0.2}Y_{0.2}Hf_{0.2}Zr_{0.2}O_2$(Y-HEC) NPs sol was synthesized via a co-precipitation method, and the sensor was fabricated by applying Y-HEC onto an indium tin oxide (ITO) electrode via a drop-coating technique. These chemiresistive sensors have a range of capabilities, including broad-spectrum CO_2 gas detection (250–10000 ppm), rapid response and recovery times (49–200 s), a high repeatability, robust long-term stability, and operation at room temperature. The enhanced sensing response was attributed to the optimized Schottky barrier height at the ITO and Y-HEC interfaces, where the adsorption of nonreactive CO_2 gas on Y-HEC causes a downward shift in the conduction band (CB) level owing to the surface charge transfer. This leads to Schottky barrier modulation (SBM) and a decrease in the Schottky barrier height (SBH), thereby facilitating a charge transfer in the sensor (Fig. 7a). Similarly, a CH_4 sensor was fabricated using $Gd_{0.2}La_{0.2}Ce_{0.2}Hf_{0.2}Zr_{0.2}O_2$(Ce-HEC) nanoparticles. As a chemiresistive sensor, Ce-HEC demonstrated a superior selectivity toward CH_4 gas (25–100 ppm) (Fig. 7b), a quick recovery time (115–195 s), long-term stability (6 months for 100 ppm CH_4 gas), operability at room temperature, and a limit of detection (LOD) of 25 ppm. Moreover, its power consumption was notably lower than that of commercial metal-oxide-based sensors, at approximately 50 nW, offering the advantages of being cost-effective and energy efficient. The enhanced detection performances of both sensors can be attributed to the porous structure of the non-agglomerated HEO nanoparticles, which provide a high surface area and intrinsic oxygen vacancies. Furthermore, because the HEO maintained its electrical conductivity at room temperature, the sensors exhibited a significantly reduced power consumption.

Bio-sensor

HEAs enhance the electrochemical immunoadsorption by providing numerous active sites through a cocktail effect and optimizing the electrical structure, thereby improving the electronic conductivity and other physicochemical properties. Additionally, nanostructured HEAs demonstrate versatility across multiple fields, potentially enhancing the immunosensor sensitivity and accuracy. Among the various types of immunosensors, label-free electrochemical immunoassays are noteworthy owing to their effectiveness in trace biomarker detection due to their compact size, high efficiency, and cost-effectiveness. For example, LV et al. introduced a label-free electrochemical amperometric immunosensor for the detection of neuron-specific enolases (NSE) [152]. They synthesized the self-supported PtPdMnCoFe high-entropy alloy with nanochain-like internetworks (HEAINN) using the one-pot co-reduction method. The developed sensor effectively reduced H_2O_2, thereby amplifying the signal and enabling the measurement of NSE. It exhibited a wide linear range from 0.1 pg mL^{-1} to 200 ng mL^{-1} for the NSE immunoassay, with an LOD of 0.0036 pg mL^{-1}, signal-to-noise ratio (S/N) of 3, and broad linear scope of 0.0001–200 ng mL^{-1}. Similarly, Tang et al. synthesized dendritic PtRhMoCoFe HEAs using a wet-chemical co-reduction method, using glucose and oleylamine as co-reducing agents [153]. The resulting HEAs were employed as electrodes to construct an electrochemical label-free biosensor for the highly sensitive detection of the cTnI (cardiac troponin I) biomarker. This sensor presented a broad linear range (0.0001–200 ng mL^{-1}), an LOD of 0.0095 pg mL^{-1}, and an acceptable recovery (102.0%) in the serum samples. Wang et al. synthesized spherical mesoporous NiCoCrFeMn HEOs for DNA sensing using the sol–gel method [147]. This DNA sensor coordinates with the probe DNA when the unsaturated metal sites of the mesoporous HEO are exposed. At this point, the probe DNA is adsorbed onto the HEO, causing fluorescence quenching (Fig. 7c). The fabricated detection exhibited a linear range from 0 to 10×10^{-9} M, with a detection limit of 0.14×10^{-9} M and an LOD of 0.16–0.20 nM. This performance can be attributed to the large surface area, controllable pore size, and

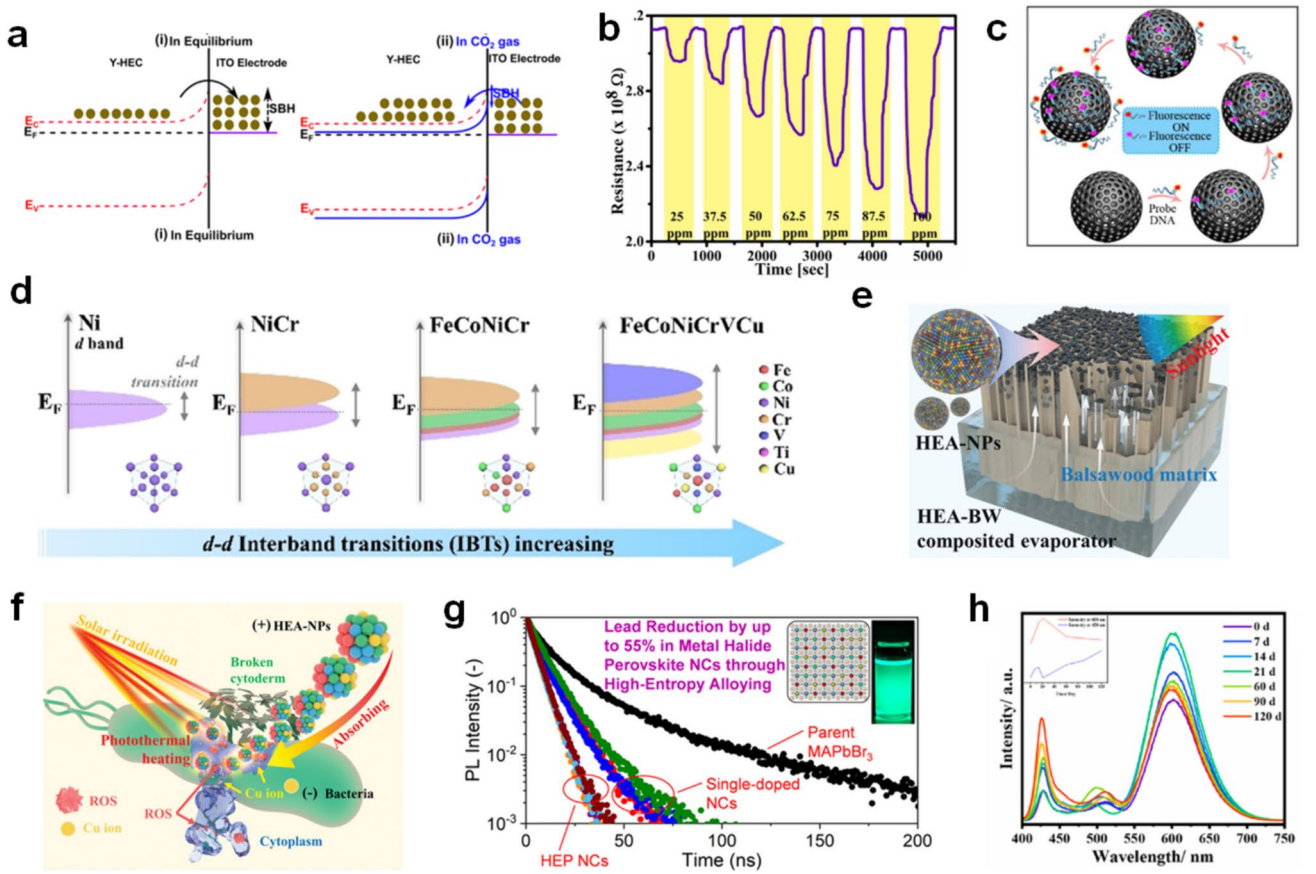

Fig. 7 **a** Schematic illustration of band bending for ITO/Y-HEC sensors under synthetic air (left) and CO_2 gas (right). Reprinted with permission from American Chemical Society [145]. **b** Dynamic resistance curves for the $Gd_{0.2}La_{0.2}Ce_{0.2}Hf_{0.2}Zr_{0.2}O_2$(Ce-HEC) sensor under exposure to CH_4 gas, with concentrations ranging from 25 to 100 ppm. Reprinted with permission from Elsevier [146]. **c** Diagram depicting the adsorption mechanism of probe DNA onto the mesoporous HEO spheres. Reprinted with permission from American Chemical Society [147]. **d** Broadening of the spectrum due to various 3d metals in HEA. Reprinted with permission from John Wiley and Sons [148]. **e** HEA-BW evaporator. Reprinted with permission from John Wiley and Sons [149]. **f** Antibacterial and antibiofilm mechanisms of HEA-NPs. Reprinted with permission from John Wiley and Sons [150]. **g** PL lifetime graph comparing bare MAPbBr3 NCs, single-doped perovskite NCs, and HEP NCs [34]. **h** Changes in the PL intensity over time at room temperature for the $Cs(Pb_{1/5}Mn_{1/5}Ni_{1/5}Zn_{1/5}Cd_{1/5})Br_3$/$Cs(Pb_{1/5}Mn_{1/5}Ni_{1/5}Zn_{1/5}Cd_{1/5})_2Br_5$ NPs. Reprinted with permission from Elsevier [151]

uniform sphere size of the superficial mesoporous HEOs. These biosensors utilize the combined benefits of a high entropy, including an increased surface area, durability, and unique structural features. Owing to the ability to produce these biosensors in large quantities via straightforward wet-chemical synthesis methods, they can be tailored for specific biomarker detection needs, thus serving various biomedical applications. In summary, HE-NPs offer promising prospects for developing high-performance biosensors with an enhanced sensitivity, selectivity, and scalability.

Photothermal Conversion

The application of HE-NPs in thermophotonic heating has recently gained significant attention. Methods such as arc plasma and magnetron sputtering are primarily utilized for the immediate formation of HE-NPs thin films owing to their convenience, cost-effectiveness, and scalability. HEAs have been reported to exhibit excellent thermal stabilities and unique absorption characteristics across various studies [154, 155]. In particular, the excellent absorption characteristics may be attributed to the strong interband transitions of the d-band electrons facilitated by the broad-spectrum inherent in HEAs (Fig. 7d) [148].

Based on these characteristics, Li et al. deposited FeCoNiTiVCrMnCu-HEA-NPs onto balsawood (BW) matrices using the arc-discharge plasma method to fabricate

evaporators for solar thermal desalination (Fig. 7e). The resulting 8-HEA-BW evaporator achieved an optical absorption of greater than 97% and demonstrated an outstanding evaporation rate of 2.58 kg m^{-2} h^{-1} at a surface temperature of 80 °C. The elements V, Mn, and Cr enhance the visible light energy range, while Ti and Cu enhance the ultraviolet energy range. Consequently, the performance of the 8-HEA, which is composed of eight elements including transition metals, was optimized. As a result, it exhibited significantly improved light absorption properties compared to nanoparticles composed of Fe, Co, and Ni [149].

Research regarding the fabrication of antimicrobial films using $FeNiTiCrMnCu_x$ HEA-NPs with photothermal properties was also conducted. The combined effect of thermal damage caused by HEA-NPs and the release of copper ions resulted in the generation of more reactive oxygen species, leading to the rupture of cell membranes and removal of biofilms (Fig. 7f). A higher proportion of Cu in the HEA resulted in a better performance, ultimately achieving a maximum biofilm eradication of 97.4% under solar irradiation for 30 min at 400 μg mL^{-1}, even without sunlight [150]. Additionally, in the field of catalysis, the application of 2D $Cu_2Zn_1Al_{0.5}Ce_5Zr_{0.5}O_x$ HEO has demonstrated a significantly higher sun-driven photothermal CO generation rate of 37.4 mmol g^{-1} h^{-1} compared to previously reported values [156].

Quantum Dot

In the field of quantum dots (QD), using HEM can reduce the use of Pb in conventional QDs and enhance their performance. Solari et al. produced high-entropy perovskite (HEP) with the maximum lead content reduced by 55%, including $MA(PbMgZnCd)Br_3$ NCs, via reaction at room temperature under ambient conditions. The synthesized HEP exhibited a blue-shifted absorption spectrum compared to that of MAPbBr3, which can be attributed to the lattice contraction during alloying. Additionally, the ηPL value increased from 75 to 95%, whereas the average PL lifetime (τ_{avg}) decreased from 27.3 to 4.6 ns (Fig. 7g). As higher ηPL and lower τ_{avg} values are preferable in most photonics applications, these results indicate that HEM enhances the optical performance of NCs [34].

Additionally, high-energy ball-milling has been used to synthesize $Cs(Pb_{1/5}Mn_{1/5}Ni_{1/5}Zn_{1/5}Cd_{1/5})Br_3$/$Cs(Pb_{1/5}Mn_{1/5}Ni_{1/5}Zn_{1/5}Cd_{1/5})_2Br_5$ HEP, which maintains an initial luminescence intensity of 109%, even after 120 days at room temperature (Fig. 7h) [151]; furthermore, $Pr_{0.42}Nd_{0.43}Gd_{0.42}Dy_{0.41}Er_{0.32}SO_2$ quantum-confined HE nanoparticles have been synthesized via a colloidal method [157]. These studies regarding HE QDs demonstrate the prospects of new nanomaterials with the combined cocktail effects of the HEM and quantum confinement, indicating their potential for application in various fields, such as photocatalysis, optoelectronics, and thermoelectric energy generation.

Conclusions and Outlook

This review primarily focuses on the synthesis of HE-NPs using wet chemistry methods and their applications. HE-NPs predominantly consist of five or more primary metals and exhibit distinctive characteristics, such as lattice distortion, sluggish elemental diffusion, a high-entropy state, and cocktail effect, thus promising versatile applications across various domains.

Wet chemical methods have various advantages and challenges in fabricating HEMs. The main wet chemistry methods mentioned above include the following. (1) Colloidal synthesis methods, including one-pot and injection approaches, offer simplicity and scalability, but lack a precise control over the size and morphology. (2) Solvothermal synthesis yields uniform crystalline nanoparticles at relatively low temperatures, allowing the formation of diverse crystal lattices and elemental combinations based on the type of solvent used. (3) Co-precipitation, involving rapid precursor reduction under optimized conditions (temperature, solution, and precipitant), ensures a uniform elemental distribution, but struggles to achieve a consistent nanoparticle size and morphology. (4) Microwave synthesis enables rapid reaction kinetics and can be combined with other synthesis methods. (5) Laser-based methods offer a rapid fabrication but require specialized equipment. Other wet chemistry methods, including molten salt and liquid shock synthesis, contribute to the synthesis of HE-NPs, further enriching the available techniques. The resulting HE-NPs exhibited diverse structural characteristics ranging from amorphous to crystalline.

HE-NPs synthesized via wet-chemical methods demonstrate potential applications in various industrial sectors, including catalysis, energy storage, sensors, photothermal conversion, and quantum dots. These applications underscore the multifaceted potential of HE-NPs. Continued exploration of these synthesis methods may drive further advancements in the development and application of HE-NPs across diverse industries.

Acknowledgements This review was supported by the National Research Foundation of Korea (NRF) grant funded by the Korean government (MSIT) (Grant No. 2020R1A5A1018052). This research was supported by the Chung-Ang University Research Scholarship Grants in 2023. This work was also supported by Samsung Electronics., Ltd (IO240215-08947-01).

Funding This work was funded by the Ministry of Science and ICT, South Korea, 2020R1A5A1018052, Samsung Electronics,

IO240215-08947-01, Chung-Ang University, and Graduate Research Scholarship in 2023.

Data availability This review includes original figures created by the authors. The data underlying these figures are available from the corresponding author upon reasonable request. All other data discussed and referenced in this review are available in the cited original publications.

Declarations

Conflict of interest The authors declare no competing financial interest.

References

1. J.-W. Yeh, S.-K. Chen, S.-J. Lin, J.-Y. Gan, T.-S. Chin, T.-T. Shun, C.-H. Tsau, S.-Y. Chang, Nanostructured high-entropy alloys with multiple principal elements: novel alloy design concepts and outcomes. Adv. Eng. Mater. **6**, 299 (2004)
2. K. Mori, N. Hashimoto, N. Kamiuchi, H. Yoshida, H. Kobayashi, H. Yamashita, Hydrogen spillover-driven synthesis of high-entropy alloy nanoparticles as a robust catalyst for co2 hydrogenation. Nat. Commun. **12**, 3884 (2021)
3. K. Zeng, J. Zhang, W. Gao, L. Wu, H. Liu, J. Gao, Z. Li, J. Zhou, T. Li, Z. Liang, B. Xu, Y. Yao, Surface-decorated high-entropy alloy catalysts with significantly boosted activity and stability. Adv. Funct. Mater. **32**, 2204643 (2022)
4. M. Liu, Z. Zhang, F. Okejiri, S. Yang, S. Zhou, S. Dai, Entropy-maximized synthesis of multimetallic nanoparticle catalysts via a ultrasonication-assisted wet chemistry method under ambient conditions. Adv. Mater. Interfaces **6**, 1900015 (2019)
5. S. Nie, L. Wu, L. Zhao, P. Zhang, Enthalpy-change driven synthesis of high-entropy perovskite nanoparticles. Nano Res. **15**, 4867 (2022)
6. A. Abdelhafiz, B. Wang, A.R. Harutyunyan, J. Li, Carbothermal shock synthesis of high entropy oxide catalysts: dynamic structural and chemical reconstruction boosting the catalytic activity and stability toward oxygen evolution reaction. Adv. Energy Mater. **12**, 2200742 (2022)
7. C. Riley, A. De La Riva, J.E. Park, S.J. Percival, A. Benavidez, E.N. Coker, R.E. Aidun, E.A. Paisley, A. Datye, S.S. Chou, A high entropy oxide designed to catalyze co oxidation without precious metals. ACS Appl. Mater. Interfaces **13**, 8120 (2021)
8. Q. Dong, M. Hong, J. Gao, T. Li, M. Cui, S. Li, H. Qiao, A.H. Brozena, Y. Yao, X. Wang, G. Chen, J. Luo, L. Hu, Rapid synthesis of high-entropy oxide microparticles. Small **18**, 2104761 (2022)
9. M. Cui, C. Yang, B. Li, Q. Dong, M. Wu, S. Hwang, H. Xie, X. Wang, G. Wang, L. Hu, High-entropy metal sulfide nanoparticles promise high-performance oxygen evolution reaction. Adv. Energy Mater. **11**, 2002887 (2021)
10. F. Li, Y. Ma, H. Wu, Q. Zhai, J. Zhao, H. Ji, S. Tang, X. Meng, Sub-3-nm high-entropy metal sulfide nanoparticles with synergistic effects as promising electrocatalysts for enhanced oxygen evolution reaction. J. Phys. Chem. C **126**, 18323 (2022)
11. J. Shi, H. Jiang, X. Hong, J. Tang, Non-noble metal high entropy sulfides for efficient oxygen evolution reaction catalysis. Appl. Surf. Sci. **642**, 158598 (2024)
12. Q. Zhao, J. Mei, W. Jin, Q. Jiang, A novel approach to the rapid synthesis of high-entropy carbide nanoparticles. J. Am. Ceram. Soc. **103**, 4733 (2020)
13. S. Niu, Z. Yang, F. Qi, Y. Han, Z. Shi, Q. Qiu, X. Han, Y. Wang, X. Du, Electrical discharge induced bulk-to-nanoparticle transformation: nano high-entropy carbide as catalysts for hydrogen evolution reaction. Adv. Funct. Mater. **32**, 2203787 (2022)
14. T. Gu, Z. Jing, F. Miao, W. Wu, Y. Zhao, H. Hou, X. Liang, High-entropy borides with frame structure: efficient electrocatalysts for oxygen evolution reaction. Int. J. Hydrog. Energy **56**, 1464 (2024)
15. R. Guo, Z. Li, L. Li, Y. Liu, R. Zheng, C. Ma, Microstructures and oxidation mechanisms of (zr0.2hf0.2ta0.2nb0.2ti0.2)b2 high-entropy ceramic. J. Eur. Ceram. Soc. **42**, 2127 (2022)
16. J.-W. Yeh, S.-J. Lin, Breakthrough applications of high-entropy materials. J. Mater. Res. **33**, 3129 (2018)
17. X. Wang, W. Guo, Y. Fu, High-entropy alloys: emerging materials for advanced functional applications. J. Mater. Chem. A. **9**, 663 (2021)
18. S. Praveen, H.S. Kim, High-entropy alloys: potential candidates for high-temperature applications—an overview. Adv. Eng. Mater. **20**, 1700645 (2018)
19. X. Chang, M. Zeng, K. Liu, L. Fu, Phase engineering of high-entropy alloys. Adv. Mater. **32**, 1907226 (2020)
20. S.S. Aamlid, M. Oudah, J. Rottler, A.M. Hallas, Understanding the role of entropy in high entropy oxides. J. Am. Chem. Soc. **145**, 5991 (2023)
21. C. Tan, H. Zhang, Wet-chemical synthesis and applications of non-layer structured two-dimensional nanomaterials. Nat. Commun. **6**, 7873 (2015)
22. T. Imaoka, K. Yamamoto, Wet-chemical strategy for atom-precise metal cluster catalysts. Bull. Chem. Soc. Jpn **92**, 941 (2019)
23. T. Yang, Y.L. Zhao, L. Fan, J. Wei, J.H. Luan, W.H. Liu, C. Wang, Z.B. Jiao, J.J. Kai, C.T. Liu, Control of nanoscale precipitation and elimination of intermediate-temperature embrittlement in multicomponent high-entropy alloys. Acta Mater. **189**, 47 (2020)
24. L. Liu, Y. Zhang, J. Han, X. Wang, W. Jiang, C.-T. Liu, Z. Zhang, P.K. Liaw, Nanoprecipitate-strengthened high-entropy alloys. Adv. Sci. **8**, 2100870 (2021)
25. M. Baghbanzadeh, L. Carbone, P.D. Cozzoli, C.O. Kappe, Microwave-assisted synthesis of colloidal inorganic nanocrystals. Angew. Chem. Int. Ed. **50**, 11312 (2011)
26. Y. Yao, Z. Huang, L.A. Hughes, J. Gao, T. Li, D. Morris, S.E. Zeltmann, B.H. Savitzky, C. Ophus, Y.Z. Finfrock, Q. Dong, M. Jiao, Y. Mao, M. Chi, P. Zhang, J. Li, A.M. Minor, R. Shahbazian-Yassar, L. Hu, Extreme mixing in nanoscale transition metal alloys. Matter. **4**, 2340 (2021)
27. T.-T. Shun, C.-H. Hung, C.-F. Lee, Formation of ordered/disordered nanoparticles in fcc high entropy alloys. J. Alloys Compd. **493**, 105 (2010)
28. M. Theibault, C.R. McCormick, S. Lang, R.E. Schaak, H.D. Abruña, High entropy sulfide nanoparticles as lithium polysulfide redox catalysts. ACS Nano **17**, 18402 (2023)
29. A. Nikam, B. Prasad, A. Kulkarni, Wet chemical synthesis of metal oxide nanoparticles: a review. CrystEngComm **20**, 5091 (2018)
30. S.A.M. Ealia and M.P. Saravanakumar, A review on the classification, characterisation, synthesis of nanoparticles and their application, *IOP conference series: materials science and engineering*, IOP Publishing, p. 032019 (2017)
31. J.H. Cha, S.H. Cho, D.H. Kim, D. Jeon, S. Park, J.W. Jung, I.D. Kim, S.Y. Choi, Flash-thermal shock synthesis of high-entropy alloys toward high-performance water splitting. Adv. Mater. **35**, 2305222 (2023)
32. M. Hao, J. Chen, J. Chen, K. Wang, J. Wang, F. Lei, P. Hao, X. Sun, J. Xie, B. Tang, Lattice-disordered high-entropy metal hydroxide nanosheets as efficient precatalysts for bifunctional electro-oxidation. J. Colloid Interface Sci. **642**, 41 (2023)
33. K. Huang, B. Zhang, J. Wu, T. Zhang, D. Peng, X. Cao, Z. Zhang, Z. Li, Y. Huang, Exploring the impact of atomic lattice

deformation on oxygen evolution reactions based on a sub-5 nm pure face-centred cubic high-entropy alloy electrocatalyst. J. Mater. Chem. A. **8**, 11938 (2020)
34. S.F. Solari, L.-N. Poon, M. Wörle, F. Krumeich, Y.-T. Li, Y.-C. Chiu, C.-J. Shih, Stabilization of lead-reduced metal halide perovskite nanocrystals by high-entropy alloying. J. Am. Chem. Soc. **144**, 5864 (2022)
35. C.M. Rost, E. Sachet, T. Borman, A. Moballegh, E.C. Dickey, D. Hou, J.L. Jones, S. Curtarolo, J.-P. Maria, Entropy-stabilized oxides. Nat. Commun. **6**, 8485 (2015)
36. A. Sarkar, B. Breitung, H. Hahn, High entropy oxides: the role of entropy, enthalpy and synergy. Scr. Mater. **187**, 43 (2020)
37. M. Coduri, M. Fracchia, M. Guerrini, C. Dejoie, P. Ghigna, U.A. Tamburini, Novel in-based high entropy spinel oxides with tunable lattice parameter. J. Eur. Ceram. Soc. **43**, 2728 (2023)
38. O.F. Dippo, K.S. Vecchio, A universal configurational entropy metric for high-entropy materials. Scr. Mater. **201**, 113974 (2021)
39. A.V. Saghir, S.M. Beidokhti, J.V. Khaki, A. Salimi, One-step synthesis of single-phase (Co, Mg, Ni, Cu, Zn) O high entropy oxide nanoparticles through SCS procedure: thermodynamics and experimental evaluation. J. Eur. Ceram. Soc. **41**, 563 (2021)
40. H. You, J. Fang, Particle-mediated nucleation and growth of solution-synthesized metal nanocrystals: a new story beyond the lamer curve. Nano Today **11**, 145 (2016)
41. W. Chen, S. Luo, M. Sun, X. Wu, Y. Zhou, Y. Liao, M. Tang, X. Fan, B. Huang, Z. Quan, High-entropy intermetallic ptrhbisnsb nanoplates for highly efficient alcohol oxidation electrocatalysis. Adv. Mater. **34**, 2206276 (2022)
42. Z. Chen, J. Wen, C. Wang, X. Kang, Convex cube-shaped pt34fe5ni20cu31mo9ru high entropy alloy catalysts toward high-performance multifunctional electrocatalysis. Small **18**, 2204255 (2022)
43. C.R. McCormick, R.E. Schaak, Simultaneous multication exchange pathway to high-entropy metal sulfide nanoparticles. J. Am. Chem. Soc. **143**, 1017 (2021)
44. G.R. Dey, C.R. McCormick, S.S. Soliman, A.J. Darling, R.E. Schaak, Chemical insights into the formation of colloidal high entropy alloy nanoparticles. ACS Nano **17**, 5943 (2023)
45. S.S. Soliman, G.R. Dey, C.R. McCormick, R.E. Schaak, Temporal evolution of morphology, composition, and structure in the formation of colloidal high-entropy intermetallic nanoparticles. ACS Nano **17**, 16147 (2023)
46. M. Kim, H. Kang, E. Hwang, Y. Park, W. Jeong, Y.J. Hwang, D.-H. Ha, Facile colloidal synthesis of transition metal (Co, Fe, and Ni)-added ir-w nps for her in acidic electrolyte. Appl. Surf. Sci. **612**, 155862 (2023)
47. Y.-K. Hong, H.T. Kim, Y. Park, W. Jeong, M. Kim, E. Hwang, Y.J. Hwang, M.-H. Lee, D.-H. Ha, Design of eu (tta) 3 phen-incorporated sio 2-coated transition metal oxide nanoparticles for efficient luminescence and magnetic performance. Nanoscale **15**, 4604 (2023)
48. C.B. Murray, C.R. Kagan, M.G. Bawendi, Synthesis and characterization of monodisperse nanocrystals and close-packed nanocrystal assemblies. Annu. Rev. Mater. Res. **30**, 545 (2000)
49. C. Moreira Da Silva, H. Amara, F. Fossard, A. Girard, A. Loiseau, V. Huc, Colloidal synthesis of nanoparticles: from bimetallic to high entropy alloys. Nanoscale **14**, 9832 (2022)
50. G.R. Dey, S.S. Soliman, C.R. McCormick, C.H. Wood, R.R. Katzbaer, R.E. Schaak, Colloidal nanoparticles of high entropy materials: Capabilities, challenges, and opportunities in synthesis and characterization. ACS Nanosci. Au. **4**, 3 (2024)
51. M. Kim, Y. Park, T. Lee, Y.-K. Hong, D.-H. Ha, Transition-metal-incorporated molybdenum phosphide nanocatalysts synthesized through post-synthetic transformation for the hydrogen evolution reaction. Int. J. Energy Res. **46**, 17668 (2022)
52. D. Huo, M.J. Kim, Z. Lyu, Y. Shi, B.J. Wiley, Y. Xia, One-dimensional metal nanostructures: from colloidal syntheses to applications. Chem. Rev. **119**, 8972 (2019)
53. Y.N. Wijaya, J. Kim, W.M. Choi, S.H. Park, M.H. Kim, A systematic study of triangular silver nanoplates: one-pot green synthesis, chemical stability, and sensing application. Nanoscale **9**, 11705 (2017)
54. C. Zhan, Y. Xu, L. Bu, H. Zhu, Y. Feng, T. Yang, Y. Zhang, Z. Yang, B. Huang, Q. Shao, X. Huang, Subnanometer high-entropy alloy nanowires enable remarkable hydrogen oxidation catalysis. Nat. Commun. **12**, 6261 (2021)
55. J. Muro-Cruces, A.G. Roca, A. López-Ortega, E. Fantechi, D. del-Pozo-Bueno, S. Estradé, F. Peiró, B. Sepúlveda, F. Pineider, C. Sangregorio, Precise size control of the growth of Fe_3O_4 nanocubes over a wide size range using a rationally designed one-pot synthesis. ACS Nano **13**, 7716 (2019)
56. H. Li, Y. Han, H. Zhao, W. Qi, D. Zhang, Y. Yu, W. Cai, S. Li, J. Lai, B. Huang, L. Wang, Fast site-to-site electron transfer of high-entropy alloy nanocatalyst driving redox electrocatalysis. Nat. Commun. **11**, 5437 (2020)
57. Y. Sun, T. Wu, Z. Bao, J. Moon, Z. Huang, Z. Chen, H. Chen, M. Li, Z. Yang, M. Chi, T.J. Toops, Z. Wu, D.-E. Jiang, J. Liu, S. Dai, Defect engineering of ceria nanocrystals for enhanced catalysis via a high-entropy oxide strategy. ACS Cent. Sci. **8**, 1081 (2022)
58. Y. Park, H. Kim, T. Lee, Y.-K. Hong, W. Jeong, S.-K. Kim, D.-H. Ha, Design of nanocatalyst for electrode structure: electrophoretic deposition of iron phosphide nanoparticles to produce a highly active hydrogen evolution reaction catalyst. Chem. Eng. J. **431**, 133217 (2022)
59. M. Li, L. Gu, T. Li, S. Hao, F. Tan, D. Chen, D. Zhu, Y. Xu, C. Sun, Z. Yang, Tio2-seeded hydrothermal growth of spherical batio3 nanocrystals for capacitor energy-storage application. Crystals **10**, 202 (2020)
60. X. Yu, B. Wang, C. Wang, C. Zhuang, Y. Yao, Z. Li, C. Wu, J. Feng, Z. Zou, 2D high-entropy hydrotalcites. Small **17**, 2103412 (2021)
61. Z.G. Wu, L. Li, Z.M. Ren, L.C. Lv, Synthesis of palladium nanosquares by polyol-hydrothermal method. Inorg. Chem. Commun. **107**, 107498 (2019)
62. S. Hanabata, K. Kusada, T. Yamamoto, T. Toriyama, S. Matsumura, S. Kawaguchi, Y. Kubota, Y. Nishida, M. Haneda, H. Kitagawa, Denary high-entropy oxide nanoparticles synthesized by a continuous supercritical hydrothermal flow process. J. Am. Chem. Soc. **146**, 181 (2024)
63. F. Li, S.-K. Sun, Y. Chen, T. Naka, T. Hashishin, J. Maruyama, H. Abe, Bottom-up synthesis of 2d layered high-entropy transition metal hydroxides. Nanoscale Adv. **4**, 2468 (2022)
64. F. Li, G.-J. Zhang, H. Abe, Sintering of high-entropy nanoparticles obtained by polyol process: a case study of (la0.2y0.2nd0.2 sm0.2gd0.2)2ce2o7-δ. J. Eur. Ceram. Soc. **42**, 7538 (2022)
65. R.I. Walton, Perovskite oxides prepared by hydrothermal and solvothermal synthesis: a review of crystallisation, chemistry, and compositions. Chem. Eur. J. **26**, 9041 (2020)
66. M. Sethi, U.S. Shenoy, S. Muthu, D.K. Bhat, Facile solvothermal synthesis of $NiFe_2O_4$ nanoparticles for high-performance supercapacitor applications. Front. Mater. Sci. **14**, 120 (2020)
67. R. Ghasemi, B.K. Moghadas, I. Mohammadi, Solvothermal synthesis of Pd10–Ni45–Co45/rGO composites as novel electrocatalysts for enhancement of the performance of dbfc. Int. J. Hydrog. Energy **45**, 21808 (2020)

68. A. Selmani, D. Kovačević, K. Bohinc, Nanoparticles: from synthesis to applications and beyond. Adv. Colloid Interface Sci. **303**, 102640 (2022)
69. N. Nandihalli, D.H. Gregory, T. Mori, Energy-saving pathways for thermoelectric nanomaterial synthesis: hydrothermal/solvothermal, microwave-assisted, solution-based, and powder processing. Adv. Sci. **9**, 2106052 (2022)
70. N. Patil, R. Bhaskar, V. Vyavhare, R. Dhadge, V. Khaire, Y. Patil, Overview on methods of synthesis of nanoparticles. Int. J. Curr. Pharm. Res. **13**, 11 (2021)
71. A. Saremi, S.M. Mirkazemi, A. Sazvar, H. Rezaie, Controlling magnetic and surface properties of cobalt ferrite nanoparticles: a comparison of co-precipitation and solvothermal synthesis methods. Solid State Sci. **148**, 107432 (2024)
72. N.K.V. Nadimpalli, R. Bandyopadhyaya, V. Runkana, Thermodynamic analysis of hydrothermal synthesis of nanoparticles. Fluid Phase Equilib. **456**, 33 (2018)
73. T.X. Nguyen, J. Patra, C.-C. Tsai, W.-Y. Xuan, H.-Y.T. Chen, M.S. Dyer, O. Clemens, J. Li, S.B. Majumder, J.-K. Chang, J.-M. Ting, Secondary-phase-induced charge–discharge performance enhancement of co-free high entropy spinel oxide electrodes for li-ion batteries. Adv. Funct. Mater. **33**, 2300509 (2023)
74. J.S. Schmuckler, Solubility product constant, ksp. J. Chem. Educ. **59**, 245 (1982)
75. C. Wang, W. Liu, M. Liao, J. Weng, J. Shen, Y. Chen, Y. Du, Novel nano spinel-type high-entropy oxide (heo) catalyst for hydrogen production using ethanol steam reforming. Nanoscale **15**, 8619 (2023)
76. D. Wu, K. Kusada, T. Yamamoto, T. Toriyama, S. Matsumura, I. Gueye, O. Seo, J. Kim, S. Hiroi, O. Sakata, On the electronic structure and hydrogen evolution reaction activity of platinum group metal-based high-entropy-alloy nanoparticles. Chem. Sci. **11**, 12731 (2020)
77. T.X. Nguyen, Y.-H. Su, C.-C. Lin, J. Ruan, J.-M. Ting, A new high entropy glycerate for high performance oxygen evolution reaction. Adv. Sci. **8**, 2002446 (2021)
78. N.-H. Ting, T.X. Nguyen, C.-H. Lee, Y.-C. Chen, C.-H. Yeh, H.-Y.T. Chen, J.-M. Ting, Composition-controlled high entropy metal glycerate as high-performance electrocatalyst for oxygen evolution reaction. Appl. Mater. Today **27**, 101398 (2022)
79. T.X. Nguyen, Y.-H. Su, C.-C. Lin, J.-M. Ting, Self-reconstruction of sulfate-containing high entropy sulfide for exceptionally high-performance oxygen evolution reaction electrocatalyst. Adv. Funct. Mater. **31**, 2106229 (2021)
80. M. Moradi, F. Hasanvandian, A. Bahadoran, A. Shokri, S. Zerangnasrabad, B. Kakavandi, New high-entropy transition-metal sulfide nanoparticles for electrochemical oxygen evolution reaction. Electrochim. Acta **436**, 141444 (2022)
81. M. Bondesgaard, N.L.N. Broge, A. Mamakhel, M. Bremholm, B.B. Iversen, General solvothermal synthesis method for complete solubility range bimetallic and high-entropy alloy nanocatalysts. Adv. Funct. Mater. **29**, 1905933 (2019)
82. Y. Albadi, M.S. Ivanova, L.Y. Grunin, K.D. Martinson, M.I. Chebanenko, S.G. Izotova, V.N. Nevedomskiy, R.S. Abiev, V.I. Popkov, The influence of co-precipitation technique on the structure, morphology and dual-modal proton relaxivity of gdfeo3 nanoparticles. Inorganics **9**(5), 39 (2021)
83. F. Okejiri, Z. Zhang, J. Liu, M. Liu, S. Yang, S. Dai, Room-temperature synthesis of high-entropy perovskite oxide nanoparticle catalysts through ultrasonication-based method. Chemsuschem **13**, 111 (2020)
84. W. Rong, Y. Chen, R. Dang, K. Huang, J. Xia, B. Zhang, J. Liu, H. Meng, Q. Cao, J. Wu, Amorphous high-entropy IrRuCrFeCoNiO*x* as efficient water splitting oxygen evolution reaction electrocatalysts. J. Alloys Compd. **971**, 172786 (2024)
85. Y. Gao, Z. Qiu, Y. Lu, H. Zhou, R. Zhu, Z. Liu, H. Pang, Rational design and general synthesis of high-entropy metallic ammonium phosphate superstructures assembled by nanosheets. Inorg. Chem. **62**, 3669 (2023)
86. F. Waag, Y. Li, A.R. Ziefuß, E. Bertin, M. Kamp, V. Duppel, G. Marzun, L. Kienle, S. Barcikowski, B. Gökce, Kinetically-controlled laser-synthesis of colloidal high-entropy alloy nanoparticles. RSC Adv. **9**, 18547 (2019)
87. L. Ren, J. Liu, X. Liu, J. Luo, J. Li, Rapid synthesis of high-entropy antimonides under air atmosphere using microwave method to ultra-high energy density supercapacitors. J. Alloys Compd. **967**, 171816 (2023)
88. H. He, P. Kou, Z. Zhang, D. Wang, R. Zheng, H. Sun, Y. Liu, Z. Wang, Coupling high entropy oxide with hollow carbon spheres by rapid microwave solvothermal strategy for boosting oxygen evolution reaction. J. Colloid Interface Sci. **653**, 179 (2024)
89. Z. Li, Y. Sun, S. Ge, F. Zhu, F. Yin, L. Gu, F. Yang, P. Hu, G. Chen, K. Wang, An overview of synthesis and structural regulation of magnetic nanomaterials prepared by chemical coprecipitation. Metals. **13**, 152 (2023)
90. N. Masunga, B.B. Mamba, Y.W. Getahun, A.A. El-Gendy, K.K. Kefeni, Synthesis of single-phase superparamagnetic copper ferrite nanoparticles using an optimized coprecipitation method. Mater. Sci. Eng. **272**, 115368 (2021)
91. M. Sajid, J. Płotka-Wasylka, Nanoparticles: synthesis, characteristics, and applications in analytical and other sciences. Microchem. J. **154**, 104623 (2020)
92. H. Ji, Q. Qu, W. Zhang, L. He, A reverse coprecipitation route for preparing Na2WO2F4: Mn4+ phosphor with high yield. Ceram. Int. **49**, 11730 (2023)
93. B. Talluri, M. Aparna, N. Sreenivasulu, S. Bhattacharya, T. Thomas, High entropy spinel metal oxide (CoCrFeMnNi) 3O4 nanoparticles as a high-performance supercapacitor electrode material. J. Energy Storage **42**, 103004 (2021)
94. N. Shen, T. Li, B. Li, Y. Wang, H. Liu, C. Guo, X. Chen, J. Li, Dual-functional mediators of high-entropy Prussian blue analogues for lithiophilicity and sulfiphilicity in Li–S batteries. Nanoscale **16**(15), 7634–7644 (2024)
95. P. Wei, S. Zhao, L. Zhuang, H. Yu, Y. Qin, Y. Chu, Chemical co-precipitation synthesis of high-entropy rare-earth silicate nanopowders. J. Am. Ceram. Soc. **107**(5), 3577–3586 (2024)
96. H. Jahangiri, Y. Morova, A. Asghari Alamdari, Z. Eroğlu, A. Sennaroğlu, S. Guo, O. Metin, A. Motallebzadeh, Femtosecond laser-mediated preparation of hfnbtatizr refractory high-entropy alloy nanoparticles for photothermal therapy applications: Influence of solvent and fluence. Intermetallics **156**, 107834 (2023)
97. C. Guo, X. Hu, X. Han, Y. Gao, T. Zheng, D. Chen, X. Qiu, P. Wang, K. Xu, Y. Chen, Laser precise synthesis of oxidation-free high-entropy alloy nanoparticle libraries. J. Am. Chem. Soc. **146**(27), 18407–18417 (2024)
98. J. Johny, Y. Li, M. Kamp, O. Prymak, S.-X. Liang, T. Krekeler, M. Ritter, L. Kienle, C. Rehbock, S. Barcikowski, S. Reichenberger, Laser-generated high entropy metallic glass nanoparticles as bifunctional electrocatalysts. Nano Res. **15**, 4807 (2022)
99. B. Wang, C. Wang, X. Yu, Y. Cao, L. Gao, C. Wu, Y. Yao, Z. Lin, Z. Zou, General synthesis of high-entropy alloy and ceramic nanoparticles in nanoseconds. Nat. Synth. **1**, 138 (2022)
100. J. Tang, J. Xu, Z. Ye, X. Li, J. Luo, Microwave sintered porous cocrfenimo high entropy alloy as an efficient electrocatalyst for alkaline oxygen evolution reaction. J. Mater. Sci. Technol. **79**, 171 (2021)
101. A. Kumar, Y. Kuang, Z. Liang, X. Sun, Microwave chemistry, recent advancements, and eco-friendly microwave-assisted synthesis of nanoarchitectures and their applications: a review. Mater. Today Nano. **11**, 100076 (2020)

102. J. Wojnarowicz, T. Chudoba, W. Lojkowski, A review of microwave synthesis of zinc oxide nanomaterials: reactants, process parameters and morphologies. Nanomaterials **10**, 1086 (2020)
103. B. Diaz de Grenu, R. De los Reyes, A.M. Costero, P. Amorós, J.V. Ros-Lis, Recent progress of microwave-assisted synthesis of silica materials. Nanomaterials **10**, 1092 (2020)
104. S. Sharma, S.R. Parne, S.S.S. Panda, S. Gandi, Progress in microwave absorbing materials: a critical review. Adv. Colloid Interface Sci. **327**, 103143 (2024)
105. D. Wang, C. Duan, H. He, Z. Wang, R. Zheng, H. Sun, Y. Liu, C. Liu, Microwave solvothermal synthesis of component-tunable high-entropy oxides as high-efficient and stable electrocatalysts for oxygen evolution reaction. J. Colloid Interface Sci. **646**, 89 (2023)
106. M. Kheradmandfard, H. Minouei, N. Tsvetkov, A.K. Vayghan, S.F. Kashani-Bozorg, G. Kim, S.I. Hong, D.-E. Kim, Ultrafast green microwave-assisted synthesis of high-entropy oxide nanoparticles for li-ion battery applications. Mater. Chem. Phys. **262**, 124265 (2021)
107. S.K. Gupta, Y. Mao, A review on molten salt synthesis of metal oxide nanomaterials: status, opportunity, and challenge. Prog. Mater. Sci. **117**, 100734 (2021)
108. C. Villada, W. Ding, A. Bonk, T. Bauer, Engineering molten $MgCl_2$–KCl–NaCl salt for high-temperature thermal energy storage: review on salt properties and corrosion control strategies. Sol. Energy Mater. Sol. Cells **232**, 111344 (2021)
109. S.K. Gupta, Y. Mao, Recent developments on molten salt synthesis of inorganic nanomaterials: a review. J. Phys. Chem. C **125**, 6508 (2021)
110. Y. Kobayashi, D. Suzuki, S. Yokoyama, R. Shoji, Molten salt synthesis of high-entropy alloy alcocrfeniv nanoparticles for the catalytic hydrogenation of p-nitrophenol by $NaBH_4$. Int. J. Hydrog. Energy **47**, 3722 (2022)
111. T. Xue, X. Liu, H. Lei, H. Dai, Z. Huang, H. Zhang, One-step molten salt synthesis of high entropy oxides. Ceram. Int. **50**(11), 18294–18302 (2024)
112. S. Ning, T. Wen, B. Ye, Y. Chu, Low-temperature molten salt synthesis of high-entropy carbide nanopowders. J. Am. Ceram. Soc. **103**, 2244 (2020)
113. Y. Yang, B. Chen, J. Chen, L. Hu, M. Hu, Preparation of (VNbTaZrHf) c high-entropy carbide nanoparticles via electrodeoxidation in molten salt and their supercapacitive behaviour. Can. Metall. Q. **61**, 389 (2022)
114. D. Liu, H. Liu, S. Ning, Y. Chu, Chrysanthemum-like high-entropy diboride nanoflowers: a new class of high-entropy nanomaterials. J. Adv. Ceram. **9**, 339 (2020)
115. S. Dong, Q. Li, H. Hu, X. Zhang, Y. Li, K. Ye, W. Hou, J. He, H. Zhao, Application of rare-earth high entropy boride in electrocatalytic hydrogen evolution reaction. Appl. Surf. Sci. **615**, 156413 (2023)
116. Y. Sun, S. Dai, High-entropy materials for catalysis: A new frontier. Sci. Adv. **7**, eabg1600 (2021)
117. X. Cui, Y. Liu, X. Wang, X. Tian, Y. Wang, G. Zhang, T. Liu, J. Ding, W. Hu, Y. Chen, Rapid high-temperature liquid shock synthesis of high-entropy alloys for hydrogen evolution reaction. ACS Nano **18**, 2948 (2024)
118. G. Cao, J. Liang, Z. Guo, K. Yang, G. Wang, H. Wang, X. Wan, Z. Li, Y. Bai, Y. Zhang, Liquid metal for high-entropy alloy nanoparticles synthesis. Nature **619**, 73 (2023)
119. Y. Yao, Q. Dong, A. Brozena, J. Luo, J. Miao, M. Chi, C. Wang, I.G. Kevrekidis, Z.J. Ren, J. Greeley, High-entropy nanoparticles: Synthesis-structure-property relationships and data-driven discovery. Science **376**, eabn3103 (2022)
120. H. Minamihara, K. Kusada, D. Wu, T. Yamamoto, T. Toriyama, S. Matsumura, L.S.R. Kumara, K. Ohara, O. Sakata, S. Kawaguchi, Y. Kubota, H. Kitagawa, Continuous-flow reactor synthesis for homogeneous 1 nm-sized extremely small high-entropy alloy nanoparticles. J. Am. Chem. Soc. **144**, 11525 (2022)
121. Q. Chen, X. Han, Z. Xu, Q. Chen, Q. Wu, T. Zheng, P. Wang, Z. Wang, J. Wang, H. Li, Atomic phosphorus induces tunable lattice strain in high entropy alloys and boosts alkaline water splitting. Nano Energy **110**, 108380 (2023)
122. G. Yuan, M. Wu, L. Ruiz Pestana, Density functional theory-machine learning characterization of the adsorption energy of oxygen intermediates on high-entropy alloys made of earth-abundant metals. J. Phys. Chem. C **127**, 15809 (2023)
123. X. Lao, X. Liao, C. Chen, J. Wang, L. Yang, Z. Li, J.W. Ma, A. Fu, H. Gao, P. Guo, Pd-enriched-core/Pt-enriched-shell high-entropy alloy with face-centred cubic structure for c1 and c2 alcohol oxidation. Angew. Chem. **135**, e202304510 (2023)
124. X. Huang, G. Yang, S. Li, H. Wang, Y. Cao, F. Peng, H. Yu, Noble-metal-based high-entropy-alloy nanoparticles for electrocatalysis. J. Energy Chem. **68**, 721 (2022)
125. A.O. Moghaddam, E.A. Trofimov, Toward expanding the realm of high entropy materials to platinum group metals: a review. J. Alloys Compd. **851**, 156838 (2021)
126. G. Feng, F. Ning, J. Song, H. Shang, K. Zhang, Z. Ding, P. Gao, W. Chu, D. Xia, Sub-2 nm ultrasmall high-entropy alloy nanoparticles for extremely superior electrocatalytic hydrogen evolution. J. Am. Chem. Soc. **143**, 17117 (2021)
127. M. Wei, Y. Sun, F. Ai, S. Xi, J. Zhang, J. Wang, Stretchable high-entropy alloy nanoflowers enable enhanced alkaline hydrogen evolution catalysis. Appl. Catal. B **334**, 122814 (2023)
128. H. Li, M. Sun, Y. Pan, J. Xiong, H. Du, Y. Yu, S. Feng, Z. Li, J. Lai, B. Huang, The self-complementary effect through strong orbital coupling in ultrathin high-entropy alloy nanowires boosting ph-universal multifunctional electrocatalysis. Appl. Catal. B **312**, 121431 (2022)
129. C. Liu, H. Zhu, S. Lu, F. Duan, M. Du, High entropy alloy nitrides with integrated nanowire/nanosheet architecture for efficient alkaline hydrogen evolution reactions. New J. Chem. **45**, 22255 (2021)
130. K. Li, J. He, X. Guan, Y. Tong, Y. Ye, L. Chen, P. Chen, Phosphorus-modified amorphous high-entropy cofenicrmn compound as high-performance electrocatalyst for hydrazine-assisted water electrolysis. Small **19**, 2302130 (2023)
131. P. Zhou, D. Liu, Z. Wen, M. Chen, Q. Liu, Y. Ke, S. Li, S. Chen, C.T. Kwok, S. Wang, Quaternary-metal phosphide as electrocatalyst for efficient hydrogen evolution reaction in alkaline solution. Int. J. Hydrog. Energy **46**, 18878 (2021)
132. C. Feng, M. Chen, Y. Zhou, Z. Xie, X. Li, P. Xiaokaiti, Y. Kansha, A. Abudula, G. Guan, High-entropy nifecov disulfides for enhanced alkaline water/seawater electrolysis. J. Colloid Interface Sci. **645**, 724 (2023)
133. R. Wang, J. Huang, X. Zhang, J. Han, Z. Zhang, T. Gao, L. Xu, S. Liu, P. Xu, B. Song, Two-dimensional high-entropy metal phosphorus trichalcogenides for enhanced hydrogen evolution reaction. ACS Nano **16**, 3593 (2022)
134. T. Reier, H.N. Nong, D. Teschner, R. Schlögl, P. Strasser, Electrocatalytic oxygen evolution reaction in acidic environments – reaction mechanisms and catalysts. Adv. Energy Mater. **7**, 1601275 (2017)
135. C. Hu, K. Yue, J. Han, X. Liu, L. Liu, Q. Liu, Q. Kong, C.-W. Pao, Z. Hu, K. Suenaga, Misoriented high-entropy iridium ruthenium oxide for acidic water splitting. Sci. Adv. **9**, eadf9144 (2023)
136. B. Talluri, K. Yoo, J. Kim, High entropy spinel metal oxide $(CoCrFeMnNi)_3O_4$ nanoparticles as novel efficient electrocatalyst for methanol oxidation and oxygen evolution reactions. J. Environ. Chem. Eng. **10**, 106932 (2022)
137. S. He, V. Somayaji, M. Wang, S.-H. Lee, Z. Geng, S. Zhu, P. Novello, C.V. Varanasi, J. Liu, High entropy spinel oxide for

efficient electrochemical oxidation of ammonia. Nano Res. **15**, 4785–4791 (2022)
138. R. He, L. Yang, Y. Zhang, X. Wang, S. Lee, T. Zhang, L. Li, Z. Liang, J. Chen, J. Li, A. Ostovari-Moghaddam, J. Llorca, M. Ibáñez, J. Arbiol, Y. Xu, A. Cabot, A CrMnFeCoNi high entropy alloy boosting oxygen evolution/reduction reactions and zinc-air battery performance. Energy Storage Mater. **58**, 287 (2023)
139. X. Cao, Y. Gao, Z. Wang, H. Zeng, Y. Song, S. Tang, L. Luo, S. Gong, FeNiCrCoMn high-entropy alloy nanoparticles loaded on carbon nanotubes as bifunctional oxygen catalysts for rechargeable zinc-air batteries. ACS Appl. Mater. Interfaces **15**, 32365 (2023)
140. Q. An, S. Li, J. Zhou, S. Ji, Z. Wen, J. Sun, Novel spinel multicomponent high-entropy oxide as anode for lithium-ion batteries with excellent electrochemical performance. Adv. Eng. Mater. **25**, 2300585 (2023)
141. X. Liu, Y. Xing, K. Xu, H. Zhang, M. Gong, Q. Jia, S. Zhang, W. Lei, Kinetically accelerated lithium storage in high-entropy (LiMgCoNiCuZn)O enabled by oxygen vacancies. Small **18**, 2200524 (2022)
142. Z. Meng, X. Gong, J. Xu, X. Sun, F. Zeng, Z. Du, Z. Hao, W. Shi, S. Yu, X. Hu, H. Tian, A general strategy for preparing hollow spherical multilayer structures of oxygen-rich vacancy transition metal oxides, especially high entropy perovskite oxides. Chem. Eng. J. **457**, 141242 (2023)
143. C. Wang, J. Li, Z. Zhou, Y. Pan, Z. Yu, Z. Pei, S. Zhao, L. Wei, Y. Chen, Rechargeable zinc-air batteries with neutral electrolytes: recent advances, challenges, and prospects. EnergyChem. **3**, 100055 (2021)
144. L. Li, P. Ji, C. Geng, Y. Li, L. Meng, B. Zhou, J. Liang, J. Peng, X. Su, Facile synthesis of high-entropy (Co0.2Cr0.2Fe0.2Mn0.2Ni0.2)3O4 nanopowders and their electrochemical properties as supercapacitor electrode. J. Energy Storage **73**, 109182 (2023)
145. V.R. Naganaboina, M. Anandkumar, A.S. Deshpande, S.G. Singh, Single-phase high-entropy oxide nanoparticles for wide dynamic range detection of co2. ACS Appl. Nano Mater. **5**, 4524 (2022)
146. V.R. Naganaboina, M. Anandkumar, A.S. Deshpande, S.G. Singh, Single-phase high-entropy oxide-based chemiresistor: toward selective and sensitive detection of methane gas for real-time applications. Sens. Actuators B **357**, 131426 (2022)
147. G. Wang, J. Qin, Y. Feng, B. Feng, S. Yang, Z. Wang, Y. Zhao, J. Wei, Sol–gel synthesis of spherical mesoporous high-entropy oxides. ACS Appl. Mater. Interfaces **12**, 45155 (2020)
148. Y. Li, Y. Liao, J. Zhang, E. Huang, L. Ji, Z. Zhang, R. Zhao, Z. Zhang, B. Yang, Y. Zhang, B. Xu, G. Qin, X. Zhang, High-entropy-alloy nanoparticles with enhanced interband transitions for efficient photothermal conversion. Angew. Chem. Int. Ed. **60**, 27113 (2021)
149. Y. Li, Y. Ma, Y. Liao, L. Ji, R. Zhao, D. Zhu, X. Hu, G. Qin, H. Rong, X. Zhang, High-entropy-alloy-nanoparticles enabled wood evaporator for efficient photothermal conversion and sustainable solar desalination. Adv. Energy Mater. **12**, 2203057 (2022)
150. Y. Li, L. Yang, Y. Liao, R. Zhao, L. Ji, R. Su, D. Xu, F. Wang, Photothermal heating-assisted superior antibacterial and antibiofilm activity of high-entropy-alloy nanoparticles. Adv. Funct. Mater. **33**, 2302712 (2023)
151. S. Xue, H. Mao, J. Li, X. Sun, Z. Gong, B. Fan, G. Shao, H. Wang, H. Xu, R. Zhang, H. Lu, One-step synthesis of all-inorganic high-entropy dual-phase Cs‘b’Br_3/Cs‘b’2Br_5 perovskite nanocrystals by high-energy ball milling. Ceram. Int. **49**, 35202 (2023)
152. C.-L. Lv, C. Tang, H. Zhou, A.-J. Wang, J.-J. Feng, T.Y. Cheang, Self-supported PtPdMnCoFe high-entropy alloy with nanochain-like internetworks for ultrasensitive electrochemical immunoassay of biomarker. Sens. Actuators B **401**, 135041 (2024)
153. C. Tang, C.-L. Lv, P. Chen, A.-J. Wang, J.-J. Feng, T. Yun-Cheang, H. Xia, Dendritic quinary ptrhmocofe high-entropy alloy as a robust immunosensing nanoplatform for ultrasensitive detection of biomarker. Bioelectrochemistry **157**, 108639 (2024)
154. D.M. Yu, C.Y. He, X.L. Qiu, S.S. Zhao, H.X. Guo, G. Liu, X.H. Gao, A multilayer solar absorber coating based on NbMoTaW refractory high entropy alloy: optical properties, thermal stability, and failure mechanism. Mater. Today Energy. **21**, 100789 (2021)
155. C.-Y. He, X.-L. Qiu, D.-M. Yu, S.-S. Zhao, H.-X. Guo, G. Liu, X.-H. Gao, Greatly enhanced solar absorption via high entropy ceramic alcrtatizrn based solar selective absorber coatings. J. Materiomics. **7**, 460 (2021)
156. Y. Li, X. Bai, D. Yuan, C. Yu, X. San, Y. Guo, L. Zhang, J. Ye, Cu-based high-entropy two-dimensional oxide as stable and active photothermal catalyst. Nat. Commun. **14**, 3171 (2023)
157. B. Ward-O’Brien, P.D. McNaughter, R. Cai, A. Chattopadhyay, J.M. Flitcroft, C.T. Smith, D.J. Binks, J.M. Skelton, S.J. Haigh, D.J. Lewis, Quantum confined high-entropy lanthanide oxysulfide colloidal nanocrystals. Nano Lett. **22**, 8045 (2022)